ATAD2 mediates chromatin-bound histone chaperone turnover

Ariadni Liakopoulou[1], Fayçal Boussouar[1#], Daniel Perazza[1], Sophie Barral[1], Emeline Lambert[1], Tao Wang[1], Florent Chuffart[1], Ekaterina Bourova-Flin[1], Charlyne Gard[2], Denis Puthier[2], Sophie Rousseaux[1], Christophe Arnoult[1], André Verdel[1], Saadi Khochbin[1#]

1- Université Grenoble Alpes, INSERM U1209, CNRS UMR 5309, Institute for Advanced Biosciences, 38000, Grenoble, France

2- Aix Marseille Université, INSERM, UMR U1090, TAGC, Marseille, France

Correspondence:

Saadi Khochbin: saadi.khochbin@univ-grenoble-alpes.fr

Fayçal Boussouar: faycal.boussouar@univ-grenoble-alpes.fr

Abstract

ATAD2, a conserved protein which is predominantly expressed in embryonic stem (ES) cells and spermatogenic cells, emerges as a crucial regulator of chromatin plasticity. Our previous parallel studies conducted in both ES cells and *S. pombe* highlighted the fundamental role of ATAD2 in facilitating chromatin-bound histone chaperone turnover. Focusing on spermatogenesis, we demonstrate here that ATAD2 regulates the HIRA-dependent localization of H3.3 on the genome and influences H3.3-mediated gene transcription. Moreover, by modulating histone eviction and the assembly of protamines, ATAD2 ensures proper chromatin condensation and genome packaging in mature sperm. Disruption of *Atad2* function in mice leads to abnormal genome organization in mature spermatozoa. Together, these findings establish a previously overlooked level of chromatin dynamic regulation, governed by ATAD2-controlled histone chaperones binding to chromatin, which defines the balance between histone deposition and removal.

Introduction

Spermatogenesis involves unique and dramatic chromatin remodelling and genome reorganization events that take place in preparation for a shift from the universal nucleosome-based eukaryotic genome organization into a unique nucleoprotamine-based structure (Gaucher et al. 2010; Bao and Bedford 2016; Le Blevec et al. 2020; Okada 2022). During the last decade, important information on the molecular basis of the nucleosome-to-nucleoprotamine transition during the postmeiotic phases of spermatogenesis became available. Several testis-specific H2A, H2B and H3 histone variants replace the canonical histones, locally or globally, at different stages, starting early during the commitment of cells into meiotic and post-meiotic differentiation (Hoghoughi et al. 2018). Most of this nucleosome dismantling and assembly occurs in the absence of DNA replication. In other words, the replication-independent nucleosome assembly pathways, such as the well-documented HIRA-dependent H3.3 assembly, are expected to be critical in ensuring the necessary chromatin remodeling in these cells. Finally, hints to the functions of transition proteins (TPs), and their functional relationship with protamines (PRMs) were proposed based on the study of a specific late-expressing H2A variant, H2A.L.2 (Barral et al. 2017b). In the proposed model we suggest that TPs do not directly replace histones, but rather could be loaded on open H2A.L.2-containing nucleosomes to control PRM assembly. Nucleosome-to-nucleoprotamine transition also includes a TP-dependent pre-PRM2 processing, histone displacement by PRMs and the structuration of the nucleoprotamine-based genome organization in the mature spermatozoa (Barral et al. 2017b; Rezaei-Gazik et al. 2022). In mice, two protamines, PRM1 and PRM2, replace histones. PRM2 is initially synthesized as a precursor protein, which undergoes sequential proteolytic processing at its N-terminal region during its incorporation, ultimately producing the mature, fully processed PRM2 (Arevalo et al. 2022).

Taking into account this unique dynamic of post-meiotic cells' nucleosomes, it is expected that these cells massively express generic factors, or those predominantly expressed in spermatogenic cells that act on chromatin, including histone acetylating machineries, acetylated histone readers and histone variants and their chaperones, all of which mediate histone and non-histone protein exchanges. More specifically, the replication-independent nature of nucleosome assembly, both in cells undergoing meiosis and in post-meiotic cells,

63 strongly suggests the involvement of the chaperone / histone substrate couple, HIRA and
64 H3.3.
65 An important part of this replication-independent histone assembly and transitions in the
66 genome organizations occurs in the context of a massive histone H4 hyperacetylation in the
67 haploid spermatogenic cells, spermatids, mediated by NUT-p300/CBP histone
68 acetyltransferase complex (Shiota et al. 2018; Rousseaux et al. 2022). Hyperacetylation of
69 histone H4, especially, the double acetylation on H4K5K8 in these cells, leads to the binding
70 of H4 by the first bromodomain of BRDT and to histone replacement (Moriniere et al. 2009;
71 Gaucher et al. 2012; Goudarzi et al. 2016; Shiota et al. 2018). Additionally, Histone H4
72 hyperacetylation, especially at K5, could also be recognized by another bromodomain-
73 containing factor of unknown function in spermatogenic cells, ATAD2 (Caron et al. 2010;
74 Morozumi et al. 2016).
75 ATAD2 is a highly conserved bromodomain-containing factor that also harbours an AAA
76 ATPase domain (Boussouar et al. 2013; Cattaneo et al. 2014). Our early work showed that
77 Atad2 is predominantly expressed in ES cells, as well as in spermatogenic cells, and is
78 aberrantly activated in virtually all solid cancers (Caron et al. 2010). Although ATAD2's function
79 in cancer prompted many investigations (Liu et al. 2022), its function in its physiological
80 context of expression has remained largely overlooked. We reported the first investigations
81 of ATAD2's function in ES cells (Morozumi et al. 2016). These studies in ES cells showed that
82 ATAD2 is recruited into acetylated transcriptionally active chromatin and is critical to keep the
83 chromatin of ES cells highly dynamic, as illustrated by an ATAD2-dependent high rate of
84 histone exchange (Morozumi et al. 2016). Subsequent studies conducted by our laboratory, in
85 ES cells and in *S. pombe*, deciphered the molecular basis of this activity of ATAD2, which relies
86 on its capacity to ensure the turnover of the chromatin-bound histone chaperone, HIRA and
87 FACT (Wang et al. 2021). In addition to ES cells, *Atad2* is also highly expressed in male germ
88 cells, pointing to its potential role in the regulation of HIRA -dependent H3.3 assembly in these
89 cells, especially, in post-meiotic cells. Indeed, previous published works have highlighted the
90 important function of H3.3 assembly in meiotic and post-meiotic male genome programming
91 (van der Heijden et al. 2007; Yuen et al. 2014; Tang et al. 2015; Fontaine et al. 2022). We
92 therefore hypothesized that ATAD2-regulated HIRA-H3.3 activity would also be a critical
93 player in the post-meiotic male genome reorganization, as HIRA has been shown to be
94 essential post-fertilization (Lin et al. 2014) and during oogenesis (Nashun et al. 2015).

95 Using a lacZ tagged *Atad2* knockout (KO) mouse model, we could show that *Atad2*'s
96 expression is enhanced in post-meiotic male germ cells, ensuring a proper turnover of histone
97 H3.3, including on the sex chromosomes. More remarkably, our data demonstrate that ATAD2
98 controls the appropriate expression of a series of genes whose activity is known to be H3.3-
99 dependent in post-meiotic cells. Additionally, in the absence of ATAD2, perturbed nucleosome
100 structural organization leads to a delayed histone-to-PRM-replacement, leading to a defective
101 global final male genome compaction. Although this defect in mature spermatozoon genome
102 compaction has minimal effect on male fertility during natural reproduction, it impacts the
103 success rate of *in vitro* fertilization using spermatozoa from *Atad2* KO mice pointing to a more
104 fragile genome in these cells.
105 In summary, our work revealed a novel mechanism for the regulation of chromatin plasticity,
106 involving the control of histone chaperone actions, particularly that of HIRA, controlling the
107 proper male germ cell transcriptional regulation, genome compaction and optimal male
108 fertility.
109
110 **Results**
111 **Atad2 is predominantly expressed in haploid male germ cells**
112 *Atad2* is normally expressed in embryonic stem (ES) and spermatogenic cells and remains
113 silent in the majority of adult tissues (Caron et al. 2010; Morozumi et al. 2016). Therefore, in
114 addition to ES cells, male germ cells constitute the second cell type where the molecular basis
115 of the physiological ATAD2 activity could be investigated.
116 To decipher the function of ATAD2 during spermatogenesis, we used a mouse model
117 harboring an insertion of a *lacZ* reporter cassette between exons 11 and 12 that enables
118 splicing and fusion of the *lacZ* transgene with exon 11 of the long and short forms of *Atad2*
119 (**Fig.1A**) and production of a non-functional ATAD2-lacZ fusion protein (**Fig. 1B**), referred to as
120 *Atad2* KO in this study. Furthermore, we crossed these mice with transgenic mice expressing
121 ubiquitously Cre recombinase under *CMV* promoter, in order to remove the *neo* cassette and
122 to delete *Atad2's* exon 12 (**Fig. 1B**). In addition to the long somatic form of ATAD2, ATAD2L,
123 the mouse testis encodes a short isoform with predominant expression in spermatogenic cells
124 that we previously named ATAD2S (Caron et al. 2010). The combined LacZ fusion and *Cre*
125 *recombinase*-dependent deletion of *Atad2's* exon 12 make both ATAD2L and ATAD2S

126 indetectable with our homemade antibody, while as expected, a reduced level of both ATAD2
127 isoforms in Atad2 heterozygous cells can be observed (**Fig. 1C**).
128 The expression of *lacZ* under the control of the *Atad2* promoter allows one to visualize *Atad2*
129 gene activity in a stage-specific manner. X-gal staining of seminiferous tubule sections from
130 *Atad2* KO mice showed a remarkably high expression of *Atad2* in post-meiotic spermatogenic
131 cells (**Fig. 1D).** It is noteworthy that, as expected, no staining was observed in the wild-type
132 tubules.
133
134 **ATAD2 controls HIRA accumulation**
135 In our previous work performed in both *S. pombe* and mouse ES cells, we demonstrated the
136 crucial role for ATAD2 in HIRA-dependent histone dosage as well as in HIRA-chromatin
137 interaction. Among other discoveries, this work showed that in the absence of ATAD2, HIRA
138 becomes trapped on chromatin leading to its accumulation in ES cells, as well as in a variety
139 of cancer cell lines (Wang et al. 2021). Because of this very conserved action of ATAD2 in
140 controlling the HIRA activity, we reasoned that the ATAD2-dependent HIRA activity should be
141 particularly active during spermatogenic cell differentiation, especially, in post-meiotic cells,
142 when ATAD2 expression is highly induced (**Fig. 1D**). To test if the absence of ATAD2 could lead
143 to the accumulation of HIRA, as we previously reported in other systems, we quantified HIRA
144 in spermatogenic cells from both wild-type and *Atad2* KO mice. These investigations revealed
145 an accumulation of HIRA protein in *Atad2* KO spermatogenic cells (**Fig. 2A**), consistent with its
146 increased association with chromatin (Wang et al. 2021). We have also monitored HIRA
147 accumulation as a function of spermatogenic cells stages. Due to the strong activation of
148 *Atad2* after meiosis, in spermatids (**Fig.1D**), the ATAD2-dependent accumulation of HIRA was
149 expected to mostly occur in post-meiotic cells. Accordingly, we also compared HIRA
150 accumulation in fractionated spermatogenic cell extracts. This experiment demonstrated that,
151 in the absence of functional ATAD2, the accumulation of HIRA primarily occurs in round
152 spermatids (**Fig. 2B**). This finding is consistent with the post-meiotic activation of Atad2 and
153 its role in regulating the turnover of chromatin-bound HIRA.
154
155 **ATAD2 controls HIRA-dependent H3.3 localization**
156 We speculated that an increased presence of HIRA on chromatin in the absence of ATAD2,
157 should also be associated with increased amounts of deposited histones. Indeed, we have

158 demonstrated previously in *S. pombe* that histone gene inactivation could rescue the growth
159 arrest due to the absence of *Atad2/Abo1.* In parallel, we found that in ES cells, in the absence
160 of ATAD2, an increased nucleosome assembly occurs, even on the so-called nucleosome-free
161 region (NFR) (Wang et al. 2021).
162 Interestingly, visualization of H3.3, the major target of HIRA, by immunofluorescence, in *Atad2*
163 KO round spermatids, displayed a diffuse, intense staining (**Fig. 3**), which is normally
164 concentrated on the sex chromosomes (van der Heijden et al. 2007; Fontaine et al. 2022) in
165 the wild-type cells. Indeed, as expected and previously reported, in the wild-type round
166 spermatids, H3.3 was mostly observed in a single domain, close to the unique chromocenter
167 in these cells (**Fig. 3**, left panels). In the absence of ATAD2, in agreement with an increased
168 residence time of HIRA on chromatin in general and a reduced H3.3 turnover, an increased
169 level of H3.3 could be observed on the sex chromosome (adjacent to the chromocenter), and
170 more interestingly, on all over the genome (**Fig. 3**, right panels).
171
172 **General chromatin accessibility and transcriptional regulation by ATAD2**
173 H3.3 is known to be dynamically incorporated on a group of active genes, especially around
174 their transcriptional start sites (TSS) (de Dieuleveult et al. 2016). We therefore predicted that
175 the observed increased H3.3 residence time in the absence of ATAD2 would decrease TSS
176 regions' accessibility specially those of highly active genes. To verify this prediction, we
177 purified round spermatid fractions from wild-type and *Atad2 KO* mice testes and measured
178 the general chromatin accessibility following an ATAC-seq approach. Chromatin accessibility
179 was then assessed around the TSS of genes, which were categorized into four groups based
180 on the quartile of their mean expression from three independent transcriptomes of wild-type
181 round spermatids (**Fig. 4A**), from the top 25% most highly expressed genes (group 1) to the
182 25% least expressed genes (group 4). As predicted, the absence of ATAD2 was associated with
183 a significant decrease in TSS region accessibility of the most active genes (**Fig. 4B and 4C**),
184 supporting a role for ATAD2 in maintaining chromatin dynamics at the most highly active
185 chromatin regions.
186
187 To visualize the genes more sensitive to ATAD2-mediated chromatin remodeling that affect
188 transcription, we monitored whole genome transcriptional activity during the first

189 spermatogenic wave at day 20 post-partum (PP), when meiosis is complete, and in the first
190 post-meiotic cells that appear on 22-, 24- and 26-days PP.
191 In order to definitively confirm our working hypothesis on the ATAD2-HIRA-H3.3 functional
192 interaction, we took advantage of published H3.3-dependent transcriptomic data (Fontaine
193 et al. 2022). Indeed, the authors of this publication identified a series of genes that are mis-
194 regulated in cells with inactivated *H3.3b* gene. Because of the post-meiotic major activation
195 of *Atad2*, we specifically focussed on the gene lists that show a H3.3-dependent deregulated
196 expression in post-meiotic round spermatids.
197 In these transcriptomes, we specifically followed the expression of the published lists of genes
198 that are downregulated or upregulated in the absence of H3.3 (Fontaine et al. 2022). Very
199 interestingly, we observed that a significant number of genes (37%) that were reported to be
200 down-regulated in the absence of H3.3 (H3.3-activated genes), are upregulated in the absence
201 of ATAD2, particularly at day 26 PP, when post-meiotic cells are present in the testes (**Fig. 5A**,
202 **Fig. S1)**. Gene Set Enrichment Analysis (GSEA) applied to genes that are differentially
203 expressed between wild-type and *Atad2* KO cells at day 26 PP, confirmed that the "H3.3-
204 activated" gene set (corresponding to the published list of H3.3-activated genes) are clearly
205 enriched in *Atad2* KO cells (**Fig. 5A**, right panel).
206 This regulation can also be observed when we considered the published list of genes that were
207 up-regulated in the absence of H3.3 (H3.3-repressed genes). In this case, the absence of
208 ATAD2 led to the enhancement of the down-regulation of these genes (37%). In other words,
209 the absence of ATAD2 led to an enhancement of H3.3-dependent gene repression (**Fig. 5B,**
210 **Fig. S1**).
211 Fontaine and colleagues also reported that sex chromosome-linked genes that normally
212 undergo Meiotic Sex Chromosome Inactivation (MSCI), were up-regulated in the absence of
213 H3.3, indicating that H3.3 is required for their repression. We also investigated these genes
214 and showed that they present an enhancement of repression in the absence of ATAD2 (51%)
215 (**Fig. 5C, Fig. S1**).
216 These analyses clearly indicate that the absence of ATAD2 enhances H3.3 functions in
217 agreement with increased residence time of H3.3 in nucleosomes. Genes that require H3.3 to
218 be repressed or activated present an enhanced repression or activation, respectively, in the
219 absence of ATAD2.

220 Overall, these investigations remarkably confirmed a role for ATAD2 in regulating H3.3
221 function.
222
223 **ATAD2 is required for controlled histone eviction and PRM assembly**
224 ATAD2's involvement in HIRA-chromatin interaction mobility and its role in H3.3 assembly in
225 post-meiotic cells, along with its similar function in the control of other histone chaperones
226 like FACT (Wang et al. 2021), led us to investigate whether ATAD2 participates in controlling
227 the histone-to-protamine replacement that occurs later in these cells. The histone eviction
228 process involves a genome-wide histone H4 hyperacetylation (Shiota et al. 2018) and a TP-
229 mediated PRMs assembly, which directs histone eviction and the final packaging of the male
230 genome (Barral et al. 2017a). To test the involvement of ATAD2 in spermatogenic cell
231 chromatin reorganization, we sought to co-detect testis-specific H2B variant, TH2B
232 (Montellier et al. 2013), along with transition protein 1 (TP1) and protamine 1 (PRM1). TH2B
233 is first expressed at the commitment of spermatogenic cells into meiotic divisions and
234 progressively becomes the major H2B species of spermatogenic cell chromatin in the
235 subsequent stages (Montellier et al. 2013). As expected, the accumulation of TP1 and PRM1
236 in wild-type cells is associated with the eviction of the majority of histones, reflected by the
237 mutually exclusive labelling of TH2B and TP1/PRM1 in distinct cells (**Fig. 6A** and **6B**, *Atad2*
238 wild-type mice). In contrast, in *Atad2* KO cells, TH2B and TP1/PRM1 were co-detected in a
239 significant number of cells (**Fig. 6A** and **6B**), suggesting that the process of histone eviction is
240 disturbed. However, in *Atad2* KO cells, the initial delay in histone removal is transient, as
241 spermatids with high levels of transition protein TP1 and PRM1 eventually appear (**Fig. 6**).
242 These observations strongly suggest that, in the absence of ATAD2, the process of histone
243 eviction is also slowed down or delayed, allowing for the simultaneous detection of histones
244 and histone-replacing proteins in the same cells.
245
246 Given that NUT-CBP/p300-dependent H4 hyperacetylation, along with the expression of
247 H2A.L.2, TPs, and PRMs, is essential for histone removal, we also investigated whether the
248 observed delay in histone removal is due to defective histone acetylation, particularly at H4K5,
249 as well as disrupted cell type-specific expression and localization of H2A.L.2, TPs, and PRMs.
250 Immunohistochemical detection of H4K5ac, H2A.L.2, TP2, PRM1, and PRM2 revealed a similar

251 pattern and cell type-specific expression of the investigated proteins when comparing *Atad2*
252 KO and wild-type post-meiotic cells. (**Fig. S2**).
253 These data support the idea that the perturbed modified flexibility of histone/TP/PRM
254 chaperones does not grossly affect the other molecular events involved in the histone-to-PRM
255 replacement.
256
257 **Perturbed pre-PRM2 processing in the absence of ATAD2**
258 We have shown previously that the H2A.L.2-dependent process of incorporation of TPs into
259 nucleosomes is required for the proper processing of pre-PRM2. The abnormal overlapping
260 staining of histones, TP and protamines observed by immunofluorescence in *Atad2* KO cells,
261 suggested that TPs may not effectively mediate the pre-PRM processing. To test this
262 hypothesis, we took advantage of our specific pre-PRM2 antibody (Rezaei-Gazik et al. 2022)
263 to investigate pre-PRM2 maturation and assembly. **Figure 7A** shows that although pre-PRM2
264 is present in both wild-type and *Atad2* KO elongating spermatids, in the absence of ATAD2,
265 pre-PRM2 tends to form dense aggregates as well as fragmented genomic domains. This
266 phenomenon is also associated with an increased accumulation of pre-PRM2 protein level in
267 testis extracts of *Atad2* KO spermatogenic cells compared to wild-type cells as revealed by
268 ELISA and immunoblotting (**Fig. 7B, Fig. S3**).
269 These data provide strong evidence that ATAD2 is required to streamline the activity of
270 histone chaperones as well as other factors involved in histone exchange and TP/PRM
271 assembly.
272
273 **Defective mature spermatozoa genome organization and male fertility *in vitro***
274 We show that although the *Atad2* KO post-meiotic cells' defective chromatin organization
275 does not affect the testis histology (**Fig. S2** and **data not shown**), it impairs testis weight and
276 sperm count, which are significantly reduced in *Atad2* KO mice (**Fig. S4**)).
277 As expected, the impact of ATAD2 on HIRA function and TP/PRM assembly also has an impact
278 on proper sperm genome compaction. Indeed, mature sperm genome decompaction test
279 revealed a significant difference in the ability of the genome to resist genome decompaction
280 conditions between wild-type *Atad2* and *Atad2* KO spermatozoa (**Fig. 8A; Fig. S5**). Given that
281 spermatozoa with defective genome compaction are known to have poor success rate in *in*
282 *vitro* fertilization (Bashiri et al. 2021), we expected that spermatozoa from *Atad2* KO mice

283 would perform worse in *in vitro* fertilization assays compared to wild-type spermatozoa.
284 **Figure 8B** shows that this is, in fact, the case. However, surprisingly, fertility tests carried out
285 on sexually mature adult males revealed that *Atad2* KO male mice are fertile, with only a
286 statistically non-significant effect observed on their ability to foster pups (**Fig. 8C**), indicating
287 that *in vivo* fertilization could buffer a relatively large series of sperm genome compaction
288 defaults.
289
290 **Discussion**
291 Taking advantage of the very conserved structural features of ATAD2 and relying on the power
292 of yeast genetics, we previously discovered that ATAD2's function is mostly to control major
293 histone chaperone functions. Using a screen of the Abo1/ATAD2-dependent arrest of *S.*
294 *pombe* cell growth, we found that impressively, 11 of the 14-growth arrest suppressor strains
295 that we isolated, impacted histone chaperones or histones themselves, with 8 distinct
296 inactivating mutations in the histone chaperone HIRA complex. Furthermore, investigation of
297 ATAD2-depleted mouse ES cells showed that HIRA accumulates and remains bound to
298 nucleosomes, leading to nucleosome overloading around active gene TSSs and on the
299 normally nucleosome-free regions (NFRs) of these genes.
300 Here, we showed that *Atad2* is highly expressed in post-meiotic spermatogenic cells and that
301 in its absence, as in ES cells and in different cancer cells, HIRA accumulates. Our new data
302 suggest that in the absence of ATAD2 activity, HIRA residency time on chromatin increases
303 leading to decreased turnover and overloading of its substrate, the histone variant H3.3 (**Fig.**
304 **9**). This replication-independent histone has been first shown to assemble on the
305 transcriptionally inactive meiotic cell sex chromosomes by Peter de Boer's laboratory (van der
306 Heijden et al. 2007). Subsequent studies showed that H3.3 remained enriched on the sex
307 chromosomes also in early post-meiotic cells, usually localized close to the unique large
308 chromocenter in these cells (Fontaine et al. 2022).
309 In agreement with the proposed role for ATAD2 in the control of HIRA-dependent dynamics
310 of H3.3, we observed a more intense labelling of H3.3 on the sex bodies in round spermatids
311 and impressively, an increase in the genomic background detection of H3.3 in these cells.
312 The role of ATAD2 in the HIRA/H3.3 functions is further supported by comparing the reported
313 H3.3-dependent transcriptome with the ATAD2-dependent transcriptome identified here.

314 Indeed, in the absence of ATAD2, we observed an enhancement of H3.3-dependent gene
315 regulatory events (activation or repression), in agreement with an increased H3.3 presence
316 and hence function, in the chromatin of *Atad2* KO post-meiotic cells.
317 These investigations on ATAD2's role in post-meiotic spermatogenic cells built upon our
318 previous findings in *S. pombe* and ES cells, uncover an additional level of regulation of histone
319 turnover, which relies on the modulation of histone chaperone–chromatin interactions.
320 Previously, A. Groth's laboratory discovered that the histone chaperone DNAJC9 recruits the
321 ATPase HSP70 to provide the necessary energy to release the chaperone from chromatin
322 (Hammond et al. 2021). Considering our data on the role of the ATPase ATAD2 with respect
323 to HIRA and that of HSP70 with respect to DNAJC9, it is tempting to propose that ATP energy
324 is required for the proper function of histone chaperones in controlling histone turnover.
325 Interestingly, very recently, Song laboratory demonstrated that the *S. pombe* Abo1/ATAD2, is
326 required for ATP-dependent dissociation of the histone chaperone FACT from chromatin,
327 particularly at TSSs (Jang et al. 2024). In line with this conclusion, ChIP-seq mapping of FACT
328 in ATAD2-depleted ES cells revealed an accumulation of nucleosome-bound FACT at the TSSs
329 of active genes (Wang et al. 2021), supporting the idea that ATAD2 not only regulates the
330 dynamics of histone-bound HIRA but also that of other histone chaperones such as FACT.
331 In addition to histones, many chromatin-bound regulatory factors also need to dynamically
332 interact with chromatin and hence ATAD2 could also be involved in mediating the dynamic
333 interactions of such chromatin-bound factors. In agreement with this hypothesis, using
334 proteomics of ATAD2-bound nucleosomes in ES cells, we previously co-purified various
335 chromatin bound factors (Morozumi et al. 2016). Other AAA ATPase factors, such as p97/VCP,
336 have also been implicated in the remodeling of chromatin-bound factors. Indeed, the AAA
337 ATPase factor, p97/VCP, has been shown to remove H3 variant CENP-A (van den Berg et al.
338 2023), the chromatin trapped PARP1 (Krastev et al. 2022), trapped Ku70/80 (van den Boom et
339 al. 2016), DNA damage sensors, DDB2 and XPC (Puumalainen et al. 2014), RNA pol II (Lafon et
340 al. 2015), and other chromatin interacting factors. Similarly, ATAD2 AAA ATPase very likely
341 acts on other chromatin-bound factors than histone chaperones. However, in contrast to
342 p97/VCP, and due to its bromodomain, ATAD2 would preferentially act on H4K5 acetylated
343 chromatin regions and would specifically ensure the dynamics of H4 acetylated chromatin-
344 bound factors. Based on the data presented here, we can also include, a role for ATAD2 to
345 streamline steps involving the H2A.L.2-dependent recruitment of TPs and protamine assembly

346 and the final histone displacement in spermatids. The chaperones responsible for TP/PRM
347 assembly are not yet identified, but it is possible that ATAD2 plays a role in dissociating these
348 chaperones from their substrate proteins after the assembly process. That is why in our *Atad2*
349 KO spermatids, we observed an overlap between TP/PRM and histones. This could be due to
350 the delayed removal of chaperones bound to TPs and PRMs and the inability of pre-PRM2 to
351 be processed and hence of PRMs to efficiently replace histones. Since histone replacement
352 still occurs in the absence of ATAD2, it suggests that other AAA ATPases, such as p97/VCP,
353 may compensate for its function. However, under these conditions, although most of the
354 histone replacement takes place, our functional tests such as *in vitro* chromatin decompaction
355 and *in vitro* fertilization, strongly suggest that mature spermatozoa genome organization is
356 not fully complete and the spermatozoa nuclei remain fragile and sensitive to external
357 assaults.
358 In summary, the functional analysis of ATAD2 during its physiological expression in the post-
359 meiotic phases of spermatogenesis supports our previous conclusions regarding its role in ES
360 cells and its conserved activity in *S. pombe*. Together, these studies reveal a novel layer of
361 regulation in histone turnover and chromatin dynamics, based on the control of histone-
362 bound histone chaperone release.
363

364 **Materials and Methods**

365

366 **Animal care and breading**

367 Mice were housed at the Grenoble High Technology Animal Facility (PHTA). Mice were
368 euthanized following a procedure approved by the official ethic committee of the University
369 Grenoble Alpes (COMETH, C2EA-12). The investigators directly involved in care and breading
370 of mice had an official animal-handling authorization obtained after 2 weeks of intensive
371 training and a final formal evaluation.

372

373 **Generation of *Atad2*-KO mice**

374 *Atad2* KO mice were obtained from the International Knockout Mouse Consortium, the
375 Welcome Trust Sanger Institute, UK. The 'knockout-first' allele (tm1a) contains an IRES: *lacZ*
376 trapping cassette and a floxed human β-*actin* promoter-driven *neo* cassette inserted into the
377 intron 12 of the *Atad2* gene (Skarnes et al. 2011). We created $Atad2^{\Delta Neo\text{-}Exon\ 12}$ mice by crossing
378 mice bearing the *tm1a* allele with mice expressing Cre recombinase under the control of a
379 ubiquitous human promoter CMV. This cross results in an $Atad2^{LacZ\Delta Neo\text{-}Exon12}$ knockout mouse
380 with the first 11 exons of *Atad2* being fused to β-gal, leading to a non-functional ATAD2
381 protein depleted of its bromodomain and AAA ATPase domain.

382 For *Atad2* KO mice genotyping, multiplex PCR was used to detect LacZ cassette producing a
383 393-bp WT band and a 293-bp mutant band using primers *Atad2*_84231_F,
384 TATCCAACAAGCCTGAGCCC, *Atad2*_84231_R, CAACTGGAGCTGGGTCTTCC and Cas-R,
385 TCGTGGTATCGTTATGCGCC.

386

387 **Fertility test**

388 Fertility tests were carried out with sexually mature 3-month-old males. Five WT males and
389 five *Atad2* KO males were crossed with two C57BL6 females each, during 3 months, and the
390 litter sizes were monitored during this period.

391

392 ***In vitro* Fertilization**

393 Eggs were obtained from 6- to 7-week-old superovulated C57/BL6J females, stimulated by a
394 first injection of 7.5 UI of PMSG (Pregnant Mare Serum Gonadotropin), followed 48 hours later
395 by a second injection of 7.5 UI of HCG (Human Chorionic Gonadotropin). Fourteen hours later,

396 females were euthanized by cervical dislocation and cumulus-oocytes complexes (COCs)
397 released from the ampulla were collected in 500 µL M2 medium. Spermatozoa from wild type
398 and *Atad2* KO males were harvested by dilaceration of the cauda epididymitis and allowed to
399 swim in 1 mL M2 medium for 10 min at 37°C. Two hundred microliters of sperm were
400 transferred into 800 µL M16 /2% BSA and capacitated for 80 min at 37°C /5% CO_2. Finally,
401 300,000 sperm were simultaneously added to the COCs and incubated in M16 medium at 37°C
402 /5% CO_2. After 4 hours of incubation, unbound spermatozoa were removed by 3 successive
403 washes with 500 µL of M16. Twenty-four hours after fertilization, unfertilized eggs and two-
404 cell embryos (as an indication of successful fertilization), were scored.
405
406 **Protein extraction and Immunoblotting**
407 Proteins were extracted in 8M Urea, sonicated at 150J with a probe sonicator, mixed with 4x
408 Laemli loading buffer and heated for 5 minutes at 95 °C. Protein samples were loaded on 4-
409 12% Bis-Tris gels and migrated at 150 V for 1h30. The transfer step was realized using a
410 nitrocellulose membrane with the Bio-Rad Transfer Turbo machine. Nitrocellulose membrane
411 was blocked in 5% milk PBS-Tween 0.1% solution, washed 3 times for 10 minutes with PBS-
412 Tween 0.1% solution and incubated overnight at 4°C with specific antibodies listed in Table
413 S1. Membranes were washed 3 times for 10 minutes with PBS-Tween 0.1% solution and were
414 incubated with HRP secondary antibodies at 1/10000 dilution for 1h at RT under agitation.
415 Revelation was performed using ECL substrates and visualization was performed with the
416 Vilber Fusion FX Chemiluminescence imaging system (Vilber).
417
418 **ELISA**
419 Urea protein extracts were diluted in PBS and used to coat 96-well round-bottom plates,
420 followed by overnight incubation at 4 °C. Coating solution was removed and wells were
421 washed 3 times with washing buffer (BSA 1%, PBS-T 0,1%). Wells were blocked with blocking
422 buffer (5% BSA in PBS-T 0,1%) for 2 hours at room temperature under agitation. Blocking
423 buffer was removed and wells were washed 2 times with washing buffer. Primary antibodies
424 for pre-PRM2 (1:1000) and tubulin (1:5000) were diluted into blocking buffer, pipetted into
425 their corresponding wells and incubated overnight at 4°C under mild agitation. Wells were
426 washed 4 times with washing buffer and subsequent incubation with secondary HRP
427 antibodies, diluted 1:5000 in blocking buffer, was performed for 1 hour at room temperature

428 under mild agitation. Wells were washed 4 times with washing buffer, and TMB ELISA
429 Substrate was added to wells and incubated until the color developed, at which time Stop
430 Solution was added to the wells to stop the reaction. The signal was quantified using a plate
431 reader at 450nm.
432
433 **X-Gal staining**
434 Male mice were euthanized by cervical dislocation. Testes were dissected out, drilled in 3
435 points and incubated overnight at 4°C under agitation in fixative solution (0.5% glutaraldehyde,
436 2 mM $MgCl_2$ and 5 mM EGTA in PBS). After incubation until equilibration in an equilibration
437 buffer (30% sucrose, 2 mM $MgCl_2$ and 5mM EGTA in PBS), testes were frozen individually in
438 OCT on dry ice. Frozen blocks were sectioned at 10 µm slices on Superfrost™ slides and let
439 dry overnight. Slides were fixed with fixation buffer (0.2% glutaraldehyde, 100 mM $MgCl_2$ and
440 5 mM EGTA in PBS) for 10 min, washed with washing buffer (PBS, 0.02% NP-40, 0.01% Sodium
441 deoxycholate and 2 mM $MgCl_2$) for 5min and incubated three times in 50% Ethanol for 5 min
442 each. Then the slides were stained with staining solution (2 mM $MgCl_2$, 0.02% NP-40, 0.01%Na
443 Doc, 5 mM potassium ferricyanide, 10 mM potassium ferrocyanide and 0.5 mg/ml X-gal) in a
444 wet chamber for several hours at 37°C. The slides were then washed with washing buffer for
445 5 min and with distilled water, and a counterstaining was performed with hematoxylin. Finally,
446 the slides were washed with running tap water for several minutes and mounted with Dako
447 fluorescent mounting medium.
448
449 **Immunofluorescence staining of germ cells**
450 Staged seminiferous tubules were prepared as detailed in Gaucher et al. 2012. In order to
451 permeabilize the cells, the slides were placed in 0.5% saponin, 0.2% Triton X-100, and 1 × PBS
452 at RT for 15 min and washed for 5 min with PBS. The preparations were then incubated in 5%
453 milk, 0.2% PBS-Tween blocking buffer, at RT for 30 min under agitation. The primary
454 antibodies were diluted in 1% dry milk, 0.2% PBS-Tween buffer. The slides were incubated
455 overnight with this diluted solution of the primary antibodies in a humidified chamber at 4°C
456 and then washed three times for 5 min each in the antibodies' dilution buffer. The secondary
457 antibodies were diluted at 1:500 in the same buffer and incubated in a humidified chamber
458 for 30 min at 37°C, and then washed as for the primary antibodies. The DNA was
459 counterstained with Hoechst, and the slides were mounted using Dako fluorescent mounting

460 medium.

461 **Sperm head decompaction test**

462 Spermatozoa from wild type and *Atad2* KO males were harvested by dilaceration of the cauda
463 epididymis and allowed to swim in 1 mL M2 medium for 10 min at 37°C. The sperm-containing
464 suspension was transferred into a 1.5 ml Eppendorf tube and centrifuged at 3000 rpm for 8
465 min in 4℃. The sperm pellets were resuspended in PBS and dropped onto glass slides to
466 spread and dry at RT. The decompaction mix (50 mM DTT, 400 IU/ml heparin and 0.2% Triton
467 in PBS) was added to each dried sperm drop for 2 min and the decompaction was stopped by
468 placing the slides in 4% PFA for 15 min. Slides were washed with PBS for 5 minutes, stained
469 with DAPI, and mounted using Dako fluorescent mounting medium. Fluorescent images were
470 captured by a Zeiss inverted microscope under a 63X numeric aperture oil-immersion lens
471 (Carl Zeiss). The size of spermatozoa heads was calculated with ImageJ software.

472

473 **Spermatogenic cell fraction purification**

474 Spermatogenic cell fraction purification was performed as previously described (Shiota et al.
475 2018).

476

477 **ATAC-seq and data analysis**

478 **Library preparation**

479 Frozen nuclei from four biologically independent purified spermatid fractions were
480 centrifuged at 3000 g for 5 minutes and then washed in a 1% BSA-PBS solution. Libraries were
481 then prepared from 100,000 nuclei using the ATAC-seq Kit (Catalog No. 53150) from Active
482 Motif, following the manufacturer's protocol (version B9). After quality control (QC) with
483 Qubit and Fragment Analyzer, libraries were subsequently purified using AMPure XP
484 (Beckman Coulter, Catalog No. A63881) beads with a double size selection of 100-800 bp
485 fragments. After a second round of library QC (Qubit and Fragment Analyzer) we performed a
486 paired-end sequencing on a NextSeq 2000 device using a 200-cycle P2 flow cell.

487 Trimming

488 The raw fastq files were processed by 5' end trimming, keeping 30bp-length fragments, using
489 fastx_trimmer [http://hannonlab.cshl.edu/fastx_toolkit/. Accessed 28 Feb. 2022.], with
490 options -l 30 -Q33.

491 **Alignment**

492 The trimmed fastq files were aligned on the UCSC Mus_musculus mm10 genome using the
493 Bowtie2 aligner (Langmead and Salzberg 2012), with options –end-to-end, –no-mixed, –no-
494 discordant.

495 **Normalization**

496 The BigWig files (.bw) containing normalized integrated aligned read count signals were
497 obtained from by normalizing and smoothing bam files using bamCoverage (from deepTools
498 suite (Ramirez et al. 2014) with options: –binSize 4 –minMappingQuality 30 –normalizeUsing
499 RPM.

500 **Heatmap**

501 The normalized ChIP signal were converted into a 10bp bin matrix of the signal 500b upstream
502 and 1500b downstream protein-coding genes' TSS, using computeMatrix (from deepTools
503 suite (Ramirez et al. 2014), with options reference-point -R mm10_pc.bed –referencePoint
504 TSS –binSize 10 –beforeRegionStartLength 500 –afterRegionStartLength 1500

505 Heatmaps were generated using plotHeatmap (deepTools suite (Ramirez et al. 2014).

506

507 **RNA-seq data processing**

508 Wild-type (WT) and *Atad2* knockout (KO) homozygous males were sacrificed by cervical
509 dislocation on days 20-, 22-, 24-, and 26- postpartum (PP), after which their testes were
510 harvested. RNA was extracted using TRIzol™ reagent, followed by DNA digestion with DNase
511 I. The resulting RNA samples were used for RNA sequencing. For both WT and *Atad2* KO mice,
512 the biological replicates included 3 samples for D20, 4 samples for D22, 2 samples for D24 and
513 2 samples for D26.

514 The raw sequencing data (FASTQ files) were aligned to the UCSC mm10 mouse genome using
515 the STAR software (version 2.7.11b) (Dobin et al. 2013) to generate BAM files. Raw read counts
516 were extracted from the BAM files using HTSeq (version 2.0.5) (Anders et al. 2015) with the
517 following parameters: -t exon, -f bam, -r pos, --stranded=reverse, -m intersection-strict, and -
518 -nonunique none.

519 Normalization of read counts was performed using the DESeq2 R package (version 1.22.2)
520 (Anders and Huber 2010; Love et al. 2014). Counts were transformed into DESeq2-normalized
521 values and subsequently log-transformed using the formula log2(1 + DESeq2-normalized
522 counts). Differential expression analysis was conducted with the R package "SARTools" (Varet
523 et al. 2016).

524 Purified RNA from fractionated round spermatids were also sequenced to establish gene
525 transcriptional group quartile shown in Fig. 4. RNA purification and sequencing were
526 performed as described above.

527 **Quantification and statistical analysis**

528 Statistical analysis was performed with R and GraphPad Prism 8. The results of fertility tests
529 were analyzed by Student t-test. Pairwise Student t-test was used to analyze testis weights
530 and spermatozoa counts of same-aged mice and ratio pairwise Student t-test was used for the
531 IVF efficiency results. The results of sperm decompaction test were analyzed by two-way
532 ANOVA and Tukey's HSD post two-way ANOVA test was used to determine the significance
533 between groups. *P-values* < 0.05 were considered statistically significant: $*p < 0.05$, $**p < 0.01$,
534 $***p < 0.001$.
535

536 **Gene Set Enrichment Analysis (GSEA)**

537 Differential expression analysis and the corresponding GSEA analysis (Mootha et al. 2003;
538 Subramanian et al. 2005) were performed to compare *Atad2* KO versus *Atad2* wild-type
539 samples at days 20, 22, 24, and 26 PP. For the GSEA analysis, we used the Python package
540 "gseapy" (Fang et al. 2023) available at https://www.gsea-msigdb.org/gsea.
541 The GSEA was carried out on three custom gene sets. The first gene set, referred to as "sex
542 chromosome-linked genes", corresponds to genes located on the X and Y chromosomes. The
543 remaining two gene sets include genes identified as upregulated or downregulated in the

544 absence of histone H3.3 by Fontaine and colleagues (Fontaine et al. 2022). These gene sets
545 were designated as "post-meiotic H3.3-activated genes" and "post-meiotic H3.3-repressed
546 genes", respectively.
547
548 **Data availability**
549 The transcriptomic data generated in this study, corresponding to testes collected at different
550 days post-partum, have been deposited on GEO under the accession N°. GSE277943.
551 To review GEO accession GSE277943 go to :
552 https://www.ncbi.nlm.nih.gov/geo/query/acc.cgi?acc=GSE277943
553 Enter token wrszesqgjfkxxmx into the box.
554 Transcriptomic data from fractionated round spermatids (three biological replicates, Fig. 4A)
555 were deposited on GEO accession GSE284749. To review GEO accession GSE277943 go to:
556 https://www.ncbi.nlm.nih.gov/geo/query/acc.cgi?acc=GSE284749.
557 Enter token uzmvcaygpnydrgt into the box
558
559 ATAC-seq data generated in this study were deposited on GEO under the accession N°
560 GSE283879. To review GEO accession GSE283879, go to :
561 https://www.ncbi.nlm.nih.gov/geo/query/acc.cgi?acc=GSE283879
562 Enter token ozazwsmoxjofzkb into the box
563
564 **Manuscript preparation**
565 Parts of the text have been refined, with the help of free online tools (ChatGPT and DeepL).
566
567 **COMPETING INTEREST STATEMENT**
568 The authors declare that they have no conflict of interest.
569
570 **ACKNOWLEDGEMENTS**
571 This work was supported by ANR EpiSperm 4 (ANR-19-CE12- 0014), ANR Episperm 5 (ANR-23-
572 CE12-0028), ANR NME-CoA (ANR-23-CE14-0050) and the Cancer ITMO [Multi-Organization
573 Thematic Institute of the French Alliance for Life Sciences and Health (AVIESAN)] MIC program
574 to SK and SR. AL is a recipient of a 4th year PhD fellowship by Foundation pour la Recherche
575 Médicale (FRM). High throughput sequencing was performed at the TGML Platform,

supported by grants from Inserm, GIS IBiSA, Aix-Marseille Université. We thank Dr. Alexandra Varga for X-gal staining of testis sections. The authors thank Dr Kelly Matmati, Stroke Program Director, Rochester General Hospital, Connecticut, USA, for her critical reading of the manuscript.

AUTHOR CONTRIBUTIONS

AL: experimentation, data interpretation, writing and preparation of the manuscript, FB: supervision, experimentation, data interpretation, writing and preparation of the manuscript, management of acquisition of *Atad2* KO mouse model. SB: experimentation and the maintain of *Atad2* mouse model, EL and CA *in vitro* fertilization essays. FC and EBF transcriptomic data analyses. DePu and CG: transcriptomic data generation, SR: founding acquisition and transcriptomic analysis. DaPe and AV: experimentation and data generation and analyses. SK: conception, founding acquisition and supervision, and coordination of the whole project and writing of the manuscript.

593 **Figure legends**

594 **Liakopoulou_Fig1**

595

596

597 A

598

599

600

601

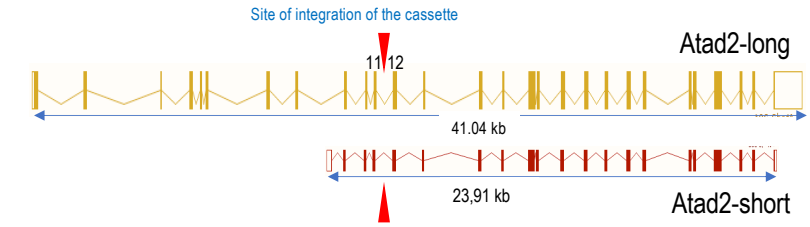

602 B

603

604

605

606

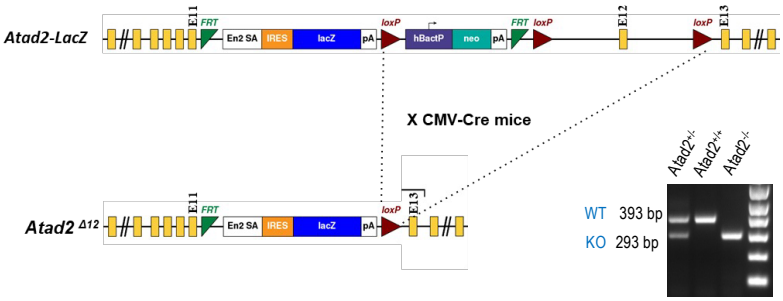

607

608 C

609

610

611

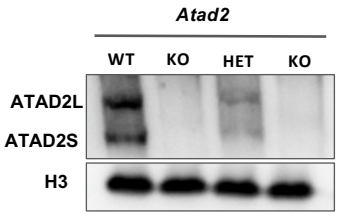

612 D

613

614

615

616

617

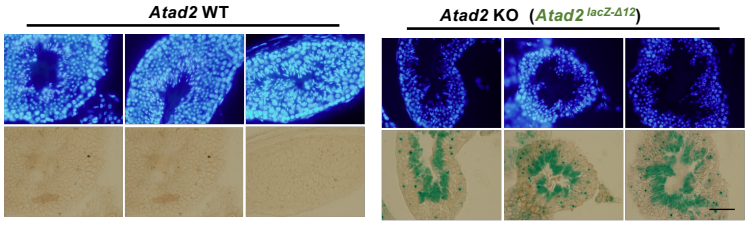

618

619 **Figure 1: *Atad2* is highly expressed in post-meiotic male germ cells.**

620 (**A**) The exon/intron organization of *Atad2* gene and the two ATAD2-encoding transcriptional

621 units (encoding for ATAD2-long and ATAD2-short) are indicated (Dyer et al. 2025). The red

622 arrows indicate the position of insertion of the *Lac-Z-Lox-Neo-Lox* cassette.

623 (**B**) Gene targeting strategy for the generation of the *Atad2* KO allele is represented. Exon

624 number and relative position, selection gene cassettes, LoxP sites and Frt sites are indicated.

625 Crossing mice bearing this construct with *CMV-Cre* mice resulted in the generation of the
626 *Atad2 LacZ*$^{\Delta Neo\text{-}Exon12}$ allele, which can be verified through PCR amplification of the genomic
627 DNA (shown on the ethidium bromide-stained gel). The expected amplified bands for each
628 genotype allowing the detection of both wild-type and KO alleles of *Atad2* are indicated. E =
629 Exon.
630 (**C**) Total protein extracts from wild-type (WT), heterozygous (HET) and *Atad2* knockout (KO)
631 mice testes were probed with anti-ATAD2 and anti-H3 antibodies as indicated. Four different
632 mice were used for this experiment.
633 (**D**) Seminiferous tubules sections from wild-type and *Atad2* KO mice were stained with X-gal
634 to visualize *lacZ* gene expression and β -galactosidase activity under the endogenous *Atad2*
635 gene promoter. Testes from three different wild-type and *Atad2* KO mice were used to
636 generate the represented sections. Scale bar: 200 µm
637
638
639
640
641
642
643
644
645
646
647
648
649
650
651
652
653
654
655
656

657 **Liakopoulou_Fig2**

658

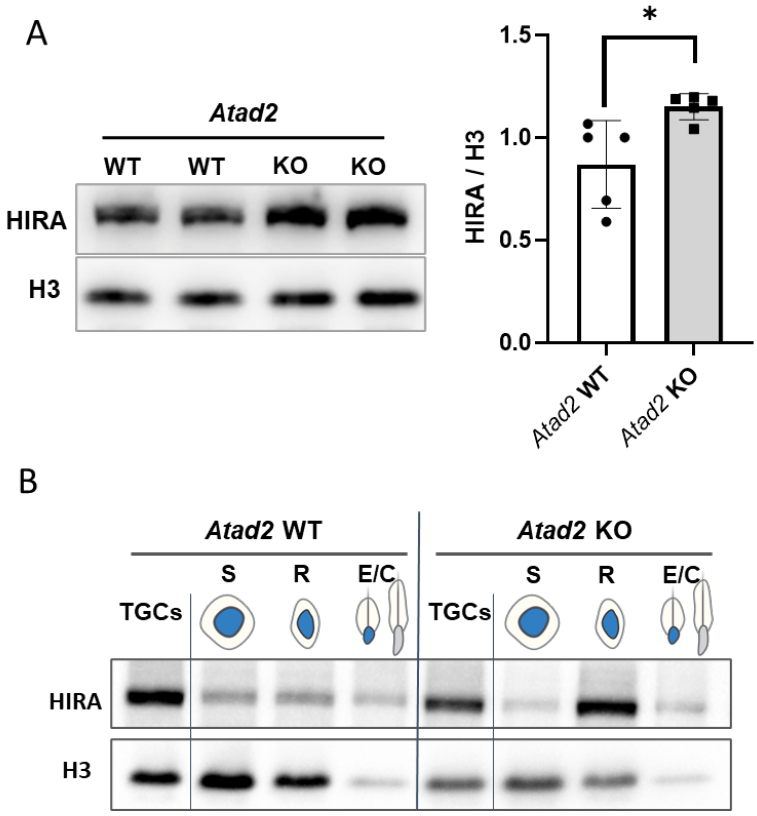

659

660 **Figure 2: *Atad2* gene inactivation leads to the accumulation of HIRA**

661 (**A**) Total protein extracts from the testes of five wild-type (WT) and five *Atad2* KO mice were
662 used to detect HIRA and H3 by immunoblotting. The panel shows a representative
663 immunoblotting after HIRA detection. The histogram in the right panel shows the
664 quantification of HIRA immunoblotting signal normalized to H3. The mean ± standard
665 deviation was 0.86± 0.21 for wild type and 1.15± 0.06 for *Atad2* KO samples. The p value was
666 0.02 for unpaired Student t-test.

667 (**B**) Protein extracts from fractionated spermatogenic cells from wild-type (*Atad2* WT) and
668 knockout (*Atad2* KO) mice (pool of testes from 3 individuals per genotype) were used to detect
669 HIRA and H3 by immunoblotting.

670

671

672

673

674

675 **Liakopoulou_Fig3**

676

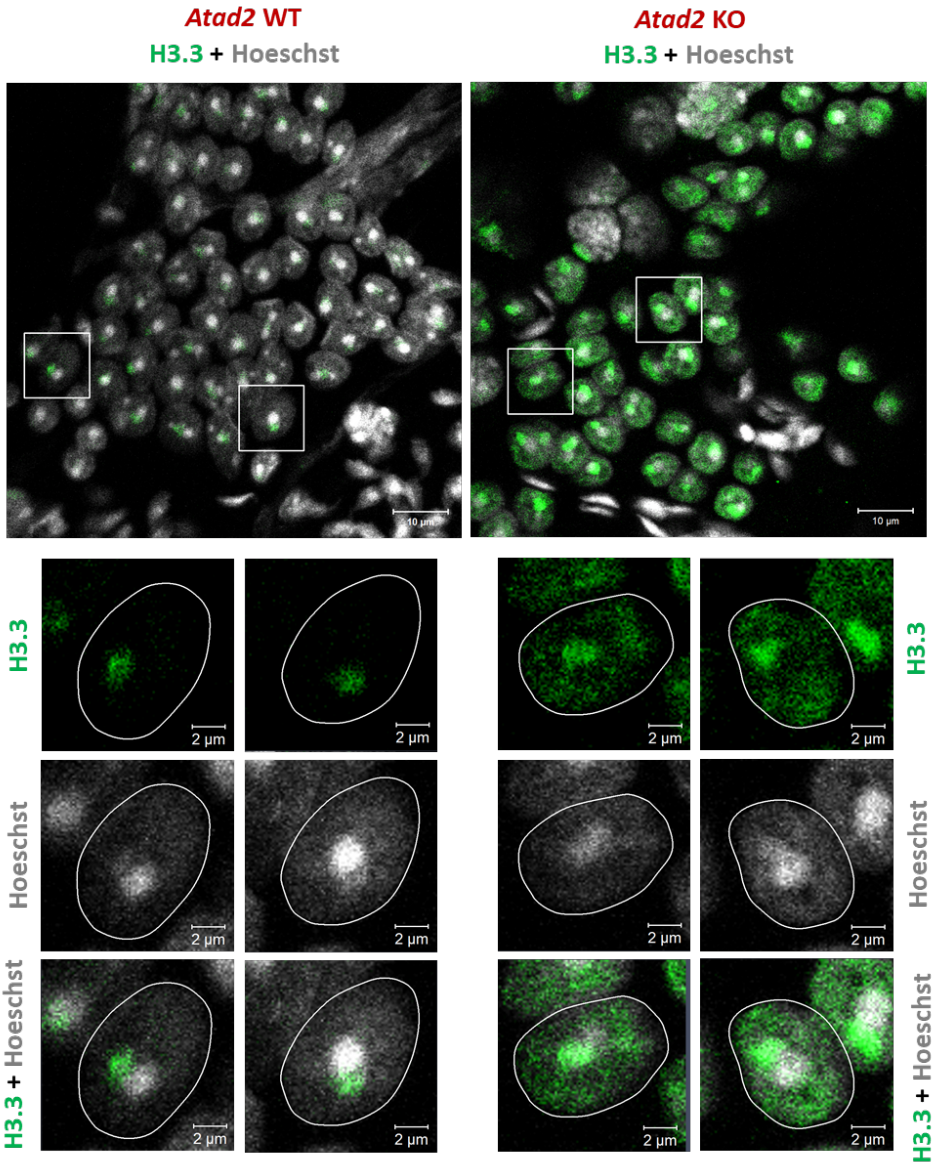

677

678 **Figure 3: Enhanced H3.3 detection in *Atad2* KO post-meiotic cells**

679 A specific antibody against H3.3 was used to detect H3.3 in round spermatid cells from wild-
680 type (*Atad2* WT) and knockout (*Atad2* KO*)* mice. Round spermatids are recognizable by their
681 distinctive Hoechst - bright chromocenter (upper panels). The lower panels represent a higher
682 magnification of selected cells that are displayed at lower magnification in the upper panels.
683 The images show H3.3 labelling and Hoechst staining alone or the merged images of these
684 staining as indicated. The nuclear boundaries defined by Hoechst staining, are outlined by
685 white lines.

686

Liakopoulou_Fig4

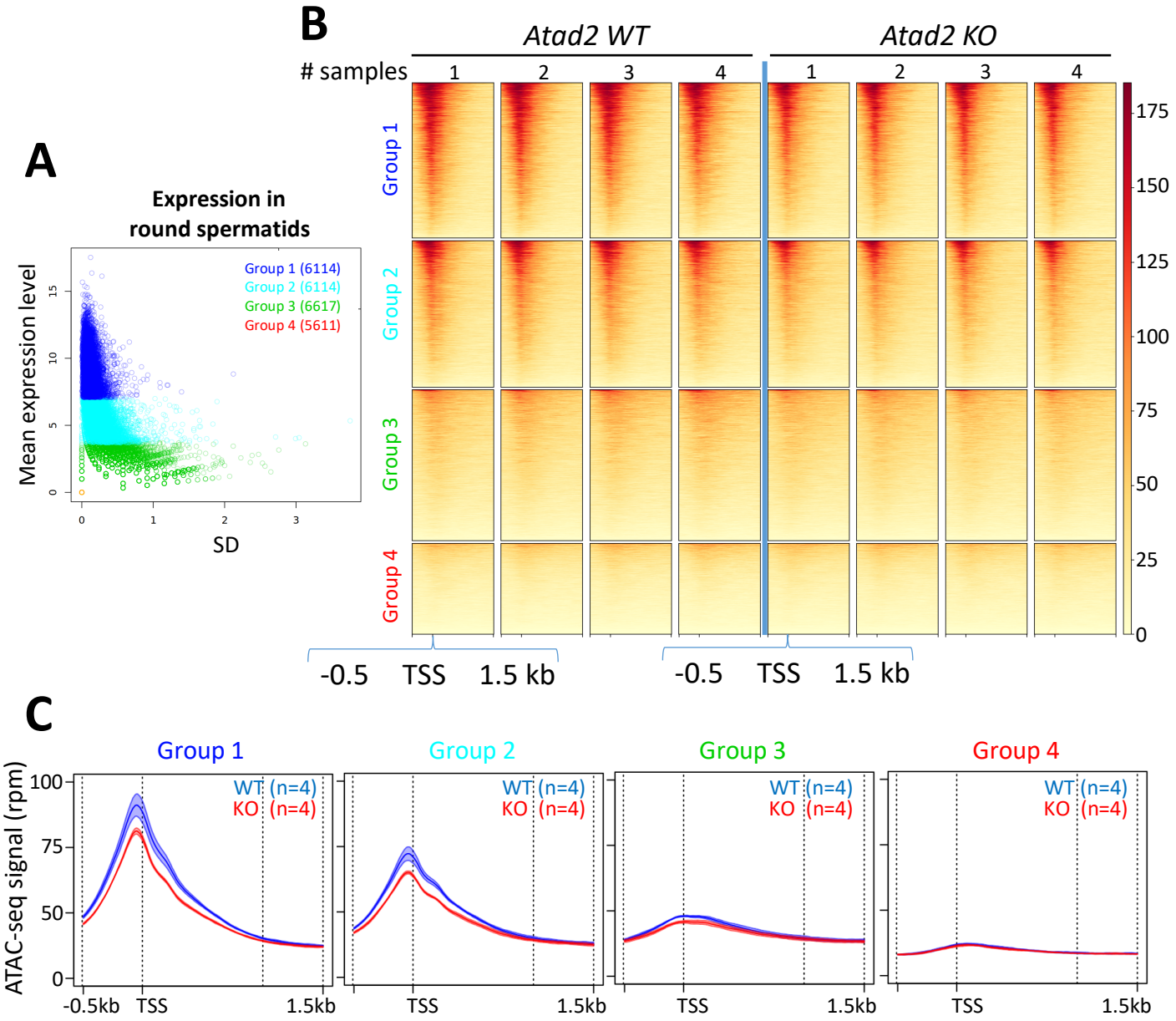

697 **Fig. 4: ATAD2 controls active gene TSS accessibility**

698 **A) Gene selection according to expression in wild-type round spermatids**. The plot displays
699 the mean expression levels (y-axis, labeled as "mean expression level") versus the correspond-
700 ing standard deviations (x-axis), both calculated from three independent biological replicates
701 of isolated round spermatids. The standard deviation reflects the variability of gene expres-
702 sion across biological replicates. Genes were grouped into four categories (Group1: blue,
703 Group 2: cyan, Group 3: green, Group 4: orange) according to the quartile of their mean ex-
704 pression. For Group 4, all genes have no detectable expression, resulting in a mean expression
705 of zero and a standard deviation of zero; consequently, the 5611 genes in this group are rep-
706 resented by a single overlapping point (red open circle) at the origin.

707 **B) Heatmap on ATAC-seq signal**. The heatmap shows the ATAC-seq signal of each group
708 (Group 1 in blue, Group 2 in cyan, Group 3 in green and Group 4 in orange) in rows, for 4 *Atad2*
709 WT and 4 *Atad2* KO samples in column.

710 **C) Profiles according to selected genes**. The mean profiles are displayed together with their
711 variability (± 2 s.e.m.) across the four replicates for both *Atad2* WT (blue) and *Atad2* KO (red).
712 For groups 1, 2, and 3, the envelopes of the curves remain clearly separated around the peak,
713 indicating a consistent difference in signal between the two conditions. In contrast, group 4
714 does not present a strong signal and, accordingly, no marked difference is observed between
715 *Atad2* WT and KO in this group.

716
717
718
719
720
721
722
723
724
725
726
727

728 **Liakopoulou_Fig5**

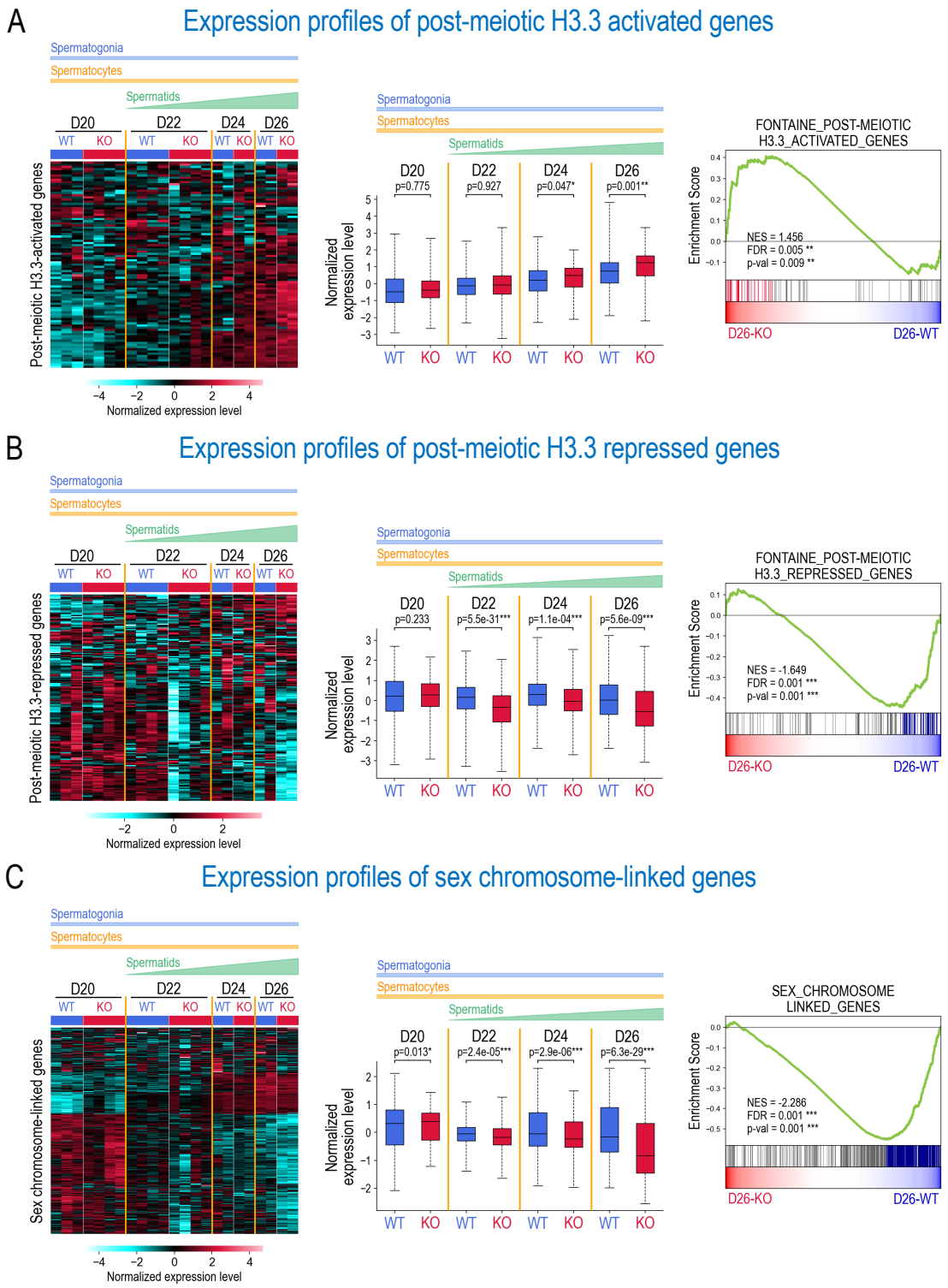

729

730 **Figure 5: ATAD2 enhances H3.3 gene regulatory functions.**

731 **(A)** Expression profiles of post-meiotic H3.3-activated genes. The heatmap (left panel) displays
732 the normalized expression levels of genes identified by Fontaine and colleagues as
733 upregulated in the absence of histone H3.3 (Fontaine et al. 2022) for *Atad2* WT (WT) and
734 *Atad2* KO (KO) samples at days 20, 22, 24, and 26 PP (D20 to D26). The colour scale represents

735 the z-score of log-transformed DESeq2-normalized counts. The middle panel box plots display,
736 pooled, normalized expression levels, aggregated across replicates and genes, for each
737 condition (WT and KO) and each time point (D20 to D26). Statistical significance between WT
738 and KO conditions was determined using a two-sided t-test, with p-values indicated as follows:
739 * for p-value<0.05, ** for p-value<0.01 and *** for p-value<0.001. The right panel shows the
740 results of gene set enrichment analysis (GSEA), which assesses whether predefined groups of
741 genes show statistically significant differences between conditions. Here, the post-meiotic
742 H3.3-activated genes set, identified by Fontaine et al. (2022), is significantly enriched in *Atad2*
743 KO compared with WT samples at day 26 ($p < 0.05$, FDR < 0.25). Coloured vertical bars indicate
744 the “leading edge” genes (i.e., those contributing most to the enrichment signal), located
745 before the point of maximum enrichment score. **(B**) As shown in (A) but for the "post-meiotic
746 H3.3-repressed genes" gene set. **(C)** As shown in (A) but for the " sex chromosome-linked
747 genes " gene set.
748
749
750
751
752
753
754
755
756
757
758
759
760
761
762
763
764

765 **Liakopoulou_Fig.6**

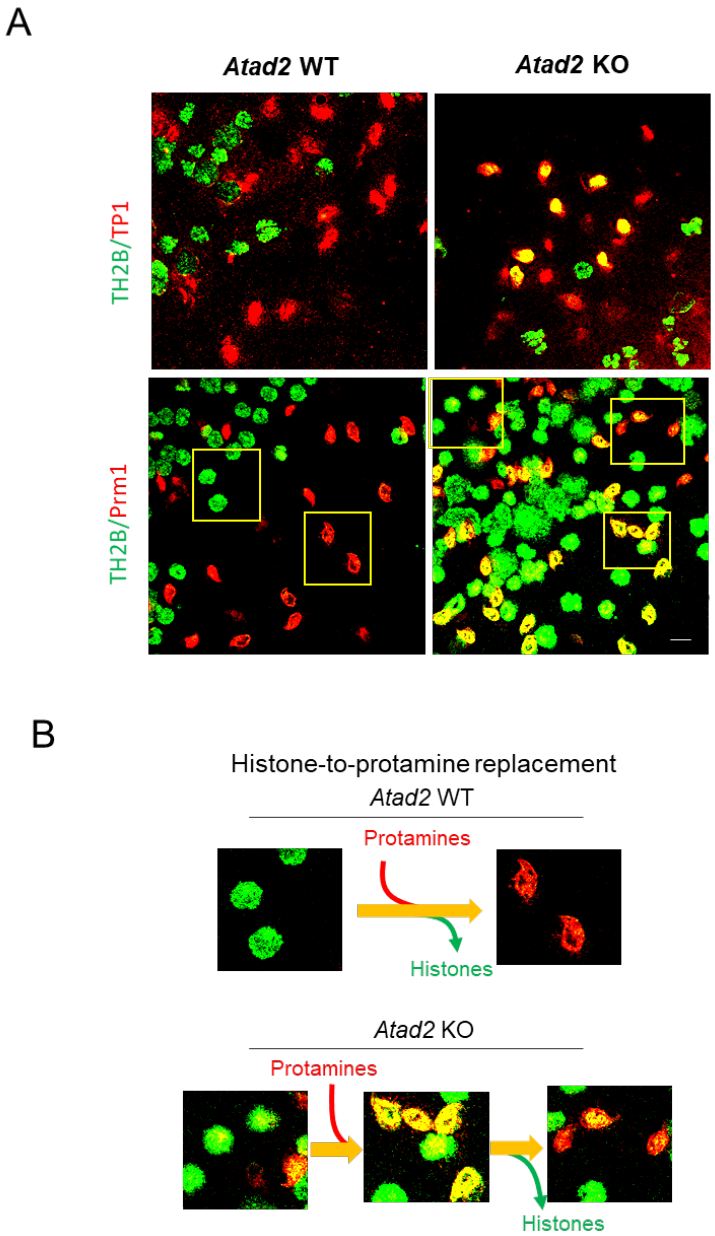

766

767 **Figure 6: ATAD2 is required for efficient histone-to-protamine replacement.**

768 (**A**) Spermatogenic cell preparations from wild-type and *Atad2* KO mice were stained with
769 antibodies against TH2B (in green) and transition protein 1 (TP1) or protamine 1 (PRM1) (in
770 red). A yellow signal indicates the co-detection of TH2B along with TP1 or PRM1. The indicated
771 fields are shown at higher magnification in panel "B". Scale bar: 10 µm.

772 (**B**) Fields shown in panel "A" are ordered to illustrate the transition from the histone
773 associated genome to its packaging by protamines, considering both wild-type and *Atad2* KO
774 spermatogenic cells.

775 **Liakopoulou_Fig. 7**

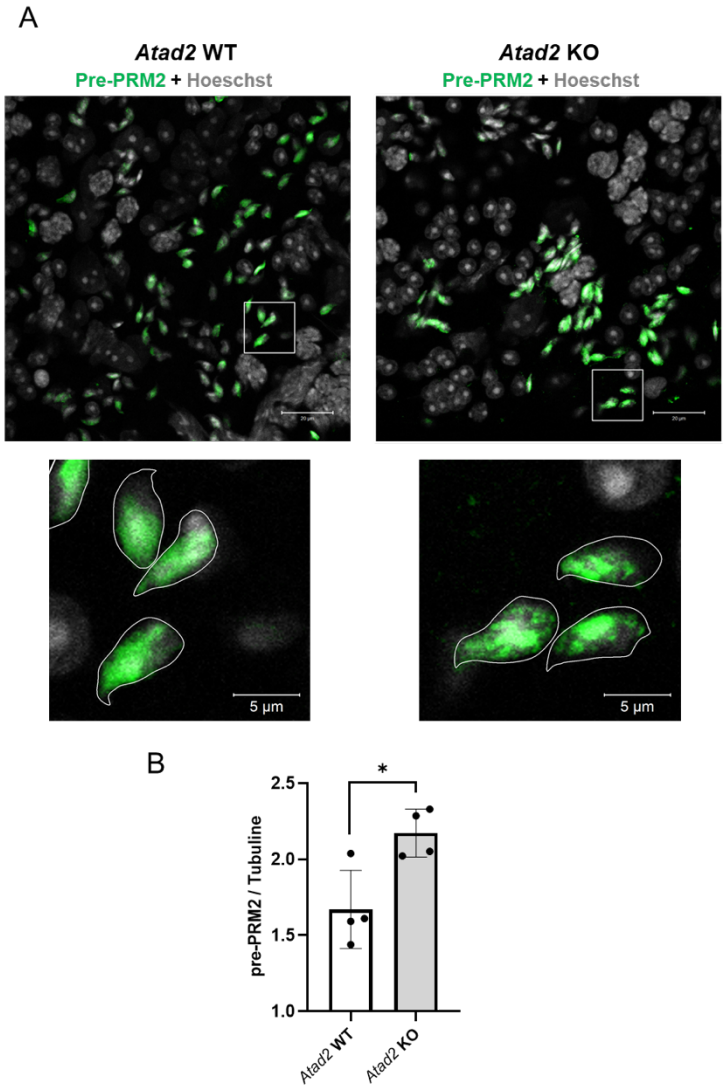

776

777 **Figure 7: ATAD2 is required for proper pre-protamine 2 processing and protamine assembly**

778 (**A**) A specific antibody raised against the processed part of pre-PRM2 (Rezaei-Gazik et al.
779 2022) was used to detect pre-PRM2 expression and localization in tubular elongating
780 spermatid cells. The lower panels represent the magnification of selected cells.

781 (**B**) The amount of pre-PRM2 was detected using soluble extracts from testis of wild-type and
782 *Atad2* KO mice using ELISA. Histograms show the normalized values (pre-PRM2/tubulin) of 4
783 measurements of independent sedimentation samples of Elongating/Condensing fractions.
784 Mean ± Standard Deviation is 1.6 ± 0.2 and 2.1 ± 0.1 for wild type and *Atad2* KO samples,
785 respectively. The p-value obtained using an unpaired Student's *t*-test was 0.0158.

786

787 **Liakopoulou_Fig8**

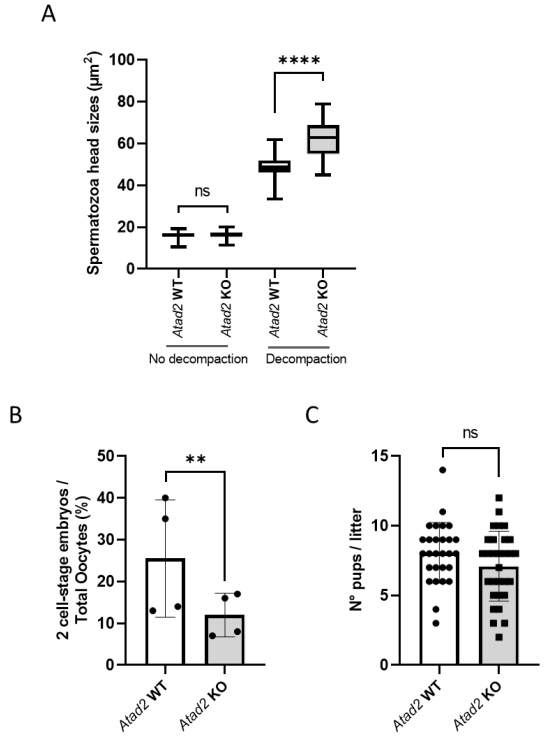

788 **Figure 8: ATAD2s' function in sperm genome compaction and fertility parameters**

789 (**A**) Epididymal sperm cells were isolated by the swim-up method from wild-type or *Atad2* KO
790 mice and underwent a decompaction test and the sizes of the sperm heads were measured
791 and represented as box plots (*n* = 75 sperm heads / box plot). The value ranges (mean) were
792 10.4 ~ 19.3 (16.0) for wild type sperms without decompaction; 11.4 ~ 20.1 (16.4) for *Atad2* KO
793 sperms without decompaction; 33.4 ~ 61.8 (48.5) for wild type sperms after decompaction;
794 45.0 ~ 78.9 (62.6) *Atad2* KO sperms after decompaction. Tukey's HSD post two-way ANOVA
795 test was used. ****$p < 0.001$.

796 (**B**) Pools of oocytes from C57BL6 females were obtained and used for *in vitro* fertilization (IVF)
797 with spermatozoa from WT or *Atad2* KO males (the experiment was repeated 4 times
798 independently). The fertilization success rate is indicated as a percentage of oocytes giving
799 rise to stage 2 embryos. Mean ± Standard Deviation is 25.5 ± 14 and 12 ± 5.2 for wild type and
800 *Atad2* KO experiments respectively and the p = 0.002 for ratio paired Student t-test.

801 (**C**) Five wild-type and five *Atad2* KO male mice were each mated with two C57BL6 females,
802 the resulting litter sizes were recorded and represented as box plots (*n* = 28 and 30,
803 respectively). The average numbers of pups are respectively 8.0 ± 2.1 and 7.1 ± 2.5 and the *p-*
804 *value of* Student t-test = 0.1.

805

806 **Liakopoulou_Fig9**

807

808 809 810 811 812 813 814 815

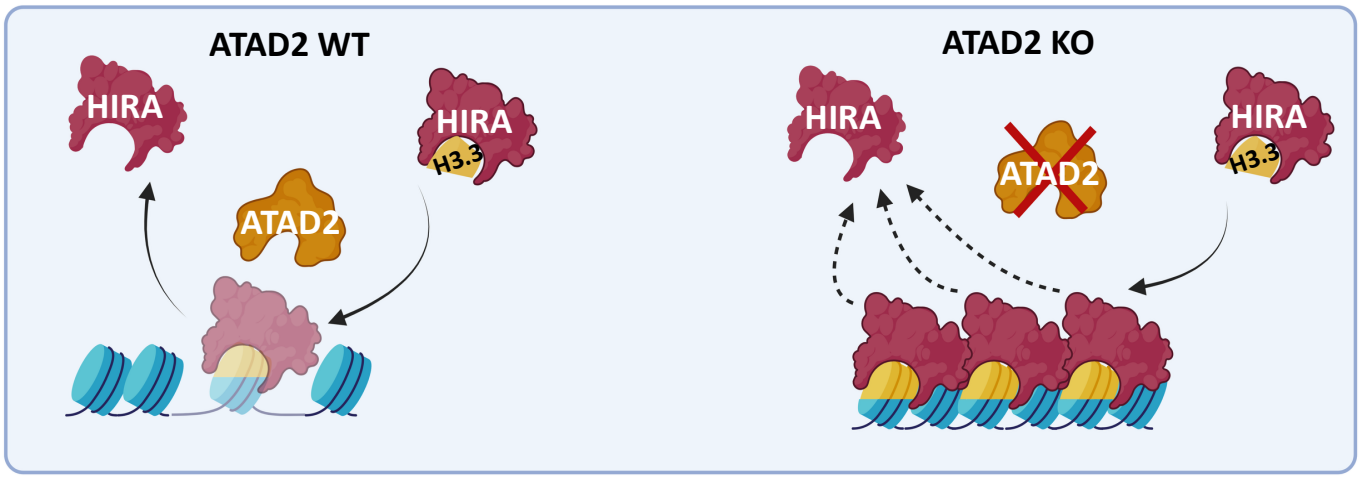

816

817 **Figure 9: A model summarizing the role of ATAD2 in regulating chromatin-bound HIRA**
818 **dynamics (along with other histone and non-histone protein chaperones) during the post-**
819 **meiotic stages of mouse spermatogenesis.** Following the deposition of H3.3 by HIRA onto
820 chromatin, ATAD2 facilitates the release of HIRA. In the absence of ATAD2, both HIRA and the
821 newly incorporated H3.3 persist longer in nucleosomes. The scheme was created using
822 BioRender.

823 824 825 826 827 828 829 830 831 832 833 834 835 836

837 **REFERENCES**

838 Anders S, Huber W. 2010. Differential expression analysis for sequence count data. *Genome*
839 *Biol* **11**: R106.
840 Anders S, Pyl PT, Huber W. 2015. HTSeq--a Python framework to work with high-throughput
841 sequencing data. *Bioinformatics* **31**: 166-169.
842 Arevalo L, Esther Merges G, Schneider S, Schorle H. 2022. Protamines: lessons learned from
843 mouse models. *Reproduction* **164**: R57-R74.
844 Bao J, Bedford MT. 2016. Epigenetic regulation of the histone-to-protamine transition during
845 spermiogenesis. *Reproduction* **151**: R55-70.
846 Barral S, Morozumi Y, Hoghoughi N, Rousseaux S, Khochbin S. 2017a. [The mystery of histone
847 disappearance during spermatogenesis]. *Med Sci (Paris)* **33**: 588-590.
848 Barral S, Morozumi Y, Tanaka H, Montellier E, Govin J, de Dieuleveult M, Charbonnier G, Coute
849 Y, Puthier D, Buchou T et al. 2017b. Histone Variant H2A.L.2 Guides Transition Protein-
850 Dependent Protamine Assembly in Male Germ Cells. *Mol Cell* **66**: 89-101 e108.
851 Bashiri Z, Amidi F, Amiri I, Zandieh Z, Maki CB, Mohammadi F, Amiri S, Koruji M. 2021. Male
852 Factors: the Role of Sperm in Preimplantation Embryo Quality. *Reprod Sci* **28**: 1788-
853 1811.
854 Boussouar F, Jamshidikia M, Morozumi Y, Rousseaux S, Khochbin S. 2013. Malignant genome
855 reprogramming by ATAD2. *Biochim Biophys Acta* **1829**: 1010-1014.
856 Caron C, Lestrat C, Marsal S, Escoffier E, Curtet S, Virolle V, Barbry P, Debernardi A, Brambilla
857 C, Brambilla E et al. 2010. Functional characterization of ATAD2 as a new cancer/testis
858 factor and a predictor of poor prognosis in breast and lung cancers. *Oncogene* **29**:
859 5171-5181.
860 Cattaneo M, Morozumi Y, Perazza D, Boussouar F, Jamshidikia M, Rousseaux S, Verdel A,
861 Khochbin S. 2014. Lessons from yeast on emerging roles of the ATAD2 protein family
862 in gene regulation and genome organization. *Mol Cells* **37**: 851-856.
863 de Dieuleveult M, Yen K, Hmitou I, Depaux A, Boussouar F, Bou Dargham D, Jounier S,
864 Humbertclaude H, Ribierre F, Baulard C et al. 2016. Genome-wide nucleosome
865 specificity and function of chromatin remodellers in ES cells. *Nature* **530**: 113-116.
866 Dobin A, Davis CA, Schlesinger F, Drenkow J, Zaleski C, Jha S, Batut P, Chaisson M, Gingeras TR.
867 2013. STAR: ultrafast universal RNA-seq aligner. *Bioinformatics* **29**: 15-21.
868 Dyer SC, Austine-Orimoloye O, Azov AG, Barba M, Barnes I, Barrera-Enriquez VP, Becker A,
869 Bennett R, Beracochea M, Berry A et al. 2025. Ensembl 2025. *Nucleic Acids Res* **53**:
870 D948-D957.
871 Fang Z, Liu X, Peltz G. 2023. GSEApy: a comprehensive package for performing gene set
872 enrichment analysis in Python. *Bioinformatics* **39**.
873 Fontaine E, Papin C, Martinez G, Le Gras S, Nahed RA, Hery P, Buchou T, Ouararhni K, Favier
874 B, Gautier T et al. 2022. Dual role of histone variant H3.3B in spermatogenesis: positive
875 regulation of piRNA transcription and implication in X-chromosome inactivation.
876 *Nucleic Acids Res* **50**: 7350-7366.
877 Gaucher J, Reynoird N, Montellier E, Boussouar F, Rousseaux S, Khochbin S. 2010. From
878 meiosis to postmeiotic events: the secrets of histone disappearance. *FEBS J* **277**: 599-
879 604.
880 Gaucher JF, Mauge C, Didry D, Guichard B, Renault L, Carlier MF. 2012. Interactions of isolated
881 C-terminal fragments of neural Wiskott-Aldrich syndrome protein (N-WASP) with actin
882 and Arp2/3 complex. *J Biol Chem* **287**: 34646-34659.

883 Goudarzi A, Zhang D, Huang H, Barral S, Kwon OK, Qi S, Tang Z, Buchou T, Vitte AL, He T et al.
884 2016. Dynamic Competing Histone H4 K5K8 Acetylation and Butyrylation Are
885 Hallmarks of Highly Active Gene Promoters. *Mol Cell* **62**: 169-180.
886 Hammond CM, Bao H, Hendriks IA, Carraro M, Garcia-Nieto A, Liu Y, Reveron-Gomez N, Spanos
887 C, Chen L, Rappsilber J et al. 2021. DNAJC9 integrates heat shock molecular chaperones
888 into the histone chaperone network. *Mol Cell* **81**: 2533-2548 e2539.
889 Hoghoughi N, Barral S, Vargas A, Rousseaux S, Khochbin S. 2018. Histone variants: essential
890 actors in male genome programming. *J Biochem* **163**: 97-103.
891 Jang J, Kang Y, Zofall M, Cho C, Grewal S, Lee JY. 2024. Abo1 ATPase facilitates the dissociation
892 of FACT from chromatin. *bioRxiv*.
893 Krastev DB, Li S, Sun Y, Wicks AJ, Hoslett G, Weekes D, Badder LM, Knight EG, Marlow R, Pardo
894 MC et al. 2022. The ubiquitin-dependent ATPase p97 removes cytotoxic trapped
895 PARP1 from chromatin. *Nat Cell Biol* **24**: 62-73.
896 Lafon A, Taranum S, Pietrocola F, Dingli F, Loew D, Brahma S, Bartholomew B, Papamichos-
897 Chronakis M. 2015. INO80 Chromatin Remodeler Facilitates Release of RNA
898 Polymerase II from Chromatin for Ubiquitin-Mediated Proteasomal Degradation. *Mol*
899 *Cell* **60**: 784-796.
900 Langmead B, Salzberg SL. 2012. Fast gapped-read alignment with Bowtie 2. *Nat Methods* **9**:
901 357-359.
902 Le Blevec E, Muronova J, Ray PF, Arnoult C. 2020. Paternal epigenetics: Mammalian sperm
903 provide much more than DNA at fertilization. *Mol Cell Endocrinol* **518**: 110964.
904 Lin CJ, Koh FM, Wong P, Conti M, Ramalho-Santos M. 2014. Hira-mediated H3.3 incorporation
905 is required for DNA replication and ribosomal RNA transcription in the mouse zygote.
906 *Dev Cell* **30**: 268-279.
907 Liu H, Wen Q, Yan S, Zeng W, Zou Y, Liu Q, Zhang G, Zou J, Zou X. 2022. Tumor-Promoting
908 ATAD2 and Its Preclinical Challenges. *Biomolecules* **12**.
909 Love MI, Huber W, Anders S. 2014. Moderated estimation of fold change and dispersion for
910 RNA-seq data with DESeq2. *Genome Biol* **15**: 550.
911 Montellier E, Boussouar F, Rousseaux S, Zhang K, Buchou T, Fenaille F, Shiota H, Debernardi A,
912 Hery P, Curtet S et al. 2013. Chromatin-to-nucleoprotamine transition is controlled by
913 the histone H2B variant TH2B. *Genes Dev* **27**: 1680-1692.
914 Mootha VK, Lindgren CM, Eriksson KF, Subramanian A, Sihag S, Lehar J, Puigserver P, Carlsson
915 E, Ridderstrale M, Laurila E et al. 2003. PGC-1alpha-responsive genes involved in
916 oxidative phosphorylation are coordinately downregulated in human diabetes. *Nat*
917 *Genet* **34**: 267-273.
918 Moriniere J, Rousseaux S, Steuerwald U, Soler-Lopez M, Curtet S, Vitte AL, Govin J, Gaucher J,
919 Sadoul K, Hart DJ et al. 2009. Cooperative binding of two acetylation marks on a
920 histone tail by a single bromodomain. *Nature* **461**: 664-668.
921 Morozumi Y, Boussouar F, Tan M, Chaikuad A, Jamshidikia M, Colak G, He H, Nie L, Petosa C,
922 de Dieuleveult M et al. 2016. Atad2 is a generalist facilitator of chromatin dynamics in
923 embryonic stem cells. *J Mol Cell Biol* **8**: 349-362.
924 Nashun B, Hill PW, Smallwood SA, Dharmalingam G, Amouroux R, Clark SJ, Sharma V, Ndjetehe
925 E, Pelczar P, Festenstein RJ et al. 2015. Continuous Histone Replacement by Hira Is
926 Essential for Normal Transcriptional Regulation and De Novo DNA Methylation during
927 Mouse Oogenesis. *Mol Cell* **60**: 611-625.

928 Okada Y. 2022. Sperm chromatin condensation: epigenetic mechanisms to compact the
929 genome and spatiotemporal regulation from inside and outside the nucleus. *Genes*
930 *Genet Syst* **97**: 41-53.
931 Puumalainen MR, Lessel D, Ruthemann P, Kaczmarek N, Bachmann K, Ramadan K, Naegeli H.
932 2014. Chromatin retention of DNA damage sensors DDB2 and XPC through loss of p97
933 segregase causes genotoxicity. *Nat Commun* **5**: 3695.
934 Ramirez F, Dundar F, Diehl S, Gruning BA, Manke T. 2014. deepTools: a flexible platform for
935 exploring deep-sequencing data. *Nucleic Acids Res* **42**: W187-191.
936 Rezaei-Gazik M, Vargas A, Amiri-Yekta A, Vitte AL, Akbari A, Barral S, Esmaeili V, Chuffart F,
937 Sadighi-Gilani MA, Coute Y et al. 2022. Direct visualization of pre-protamine 2 detects
938 protamine assembly failures and predicts ICSI success. *Mol Hum Reprod* **28**.
939 Rousseaux S, Reynoird N, Khochbin S. 2022. NUT Is a Driver of p300-Mediated Histone
940 Hyperacetylation: From Spermatogenesis to Cancer. *Cancers (Basel)* **14**.
941 Shiota H, Barral S, Buchou T, Tan M, Coute Y, Charbonnier G, Reynoird N, Boussouar F, Gerard
942 M, Zhu M et al. 2018. Nut Directs p300-Dependent, Genome-Wide H4
943 Hyperacetylation in Male Germ Cells. *Cell Rep* **24**: 3477-3487 e3476.
944 Skarnes WC, Rosen B, West AP, Koutsourakis M, Bushell W, Iyer V, Mujica AO, Thomas M,
945 Harrow J, Cox T et al. 2011. A conditional knockout resource for the genome-wide
946 study of mouse gene function. *Nature* **474**: 337-342.
947 Subramanian A, Tamayo P, Mootha VK, Mukherjee S, Ebert BL, Gillette MA, Paulovich A,
948 Pomeroy SL, Golub TR, Lander ES et al. 2005. Gene set enrichment analysis: a
949 knowledge-based approach for interpreting genome-wide expression profiles. *Proc*
950 *Natl Acad Sci U S A* **102**: 15545-15550.
951 Tang MC, Jacobs SA, Mattiske DM, Soh YM, Graham AN, Tran A, Lim SL, Hudson DF, Kalitsis P,
952 O'Bryan MK et al. 2015. Contribution of the two genes encoding histone variant h3.3
953 to viability and fertility in mice. *PLoS Genet* **11**: e1004964.
954 van den Berg SJW, East S, Mitra S, Jansen LET. 2023. p97/VCP drives turnover of SUMOylated
955 centromeric CCAN proteins and CENP-A. *Mol Biol Cell* **34**: br6.
956 van den Boom J, Wolf M, Weimann L, Schulze N, Li F, Kaschani F, Riemer A, Zierhut C, Kaiser
957 M, Iliakis G et al. 2016. VCP/p97 Extracts Sterically Trapped Ku70/80 Rings from DNA
958 in Double-Strand Break Repair. *Mol Cell* **64**: 189-198.
959 van der Heijden GW, Derijck AA, Posfai E, Giele M, Pelczar P, Ramos L, Wansink DG, van der
960 Vlag J, Peters AH, de Boer P. 2007. Chromosome-wide nucleosome replacement and
961 H3.3 incorporation during mammalian meiotic sex chromosome inactivation. *Nat*
962 *Genet* **39**: 251-258.
963 Varet H, Brillet-Gueguen L, Coppee JY, Dillies MA. 2016. SARTools: A DESeq2- and EdgeR-Based
964 R Pipeline for Comprehensive Differential Analysis of RNA-Seq Data. *PLoS One* **11**:
965 e0157022.
966 Wang T, Perazza D, Boussouar F, Cattaneo M, Bougdour A, Chuffart F, Barral S, Vargas A,
967 Liakopoulou A, Puthier D et al. 2021. ATAD2 controls chromatin-bound HIRA turnover.
968 *Life Sci Alliance* **4**.
969 Yuen BT, Bush KM, Barrilleaux BL, Cotterman R, Knoepfler PS. 2014. Histone H3.3 regulates
970 dynamic chromatin states during spermatogenesis. *Development* **141**: 3483-3494.
971

972

973

974 **Supplementary materials**

975 **Supplemental_Fig_S1**

976

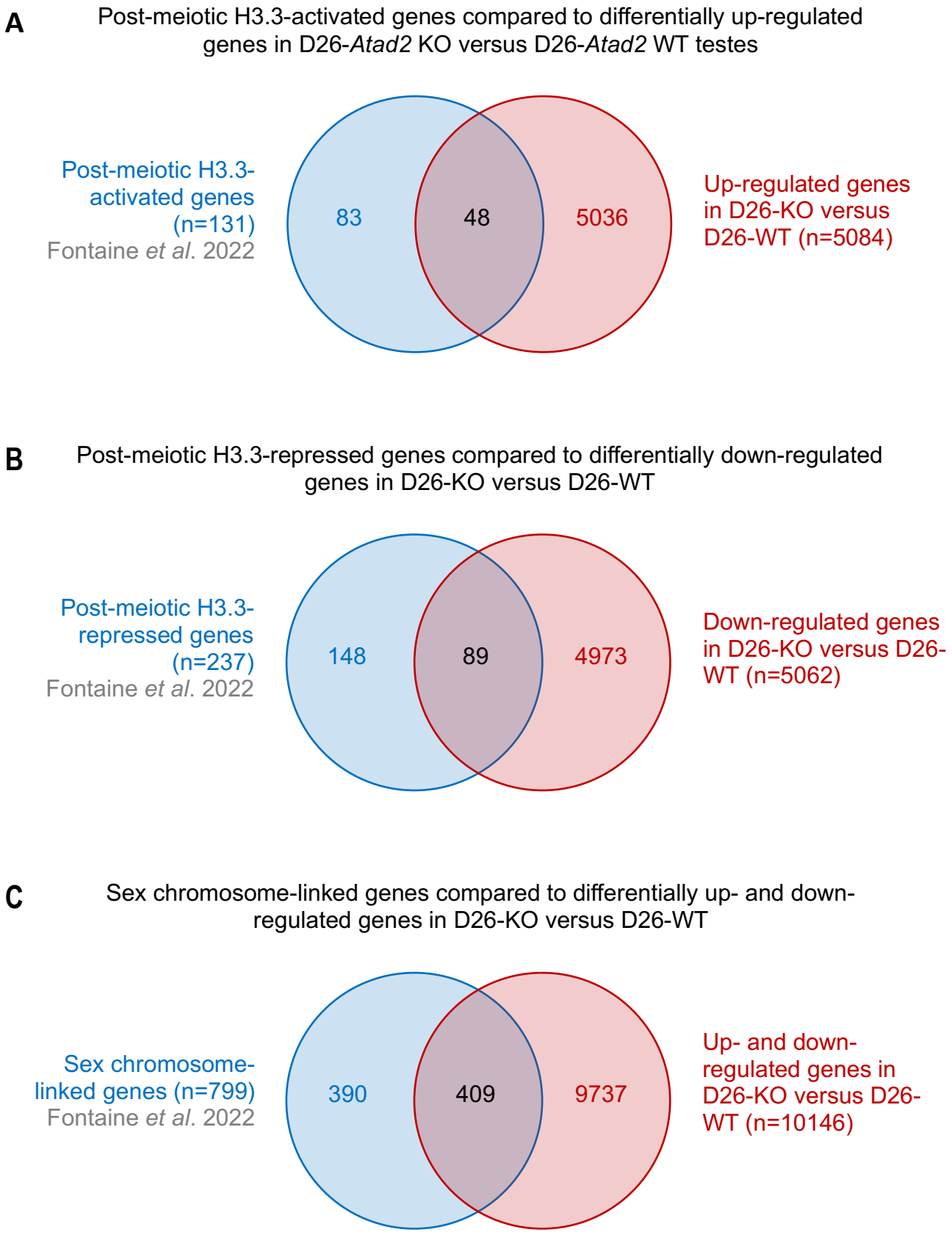

Figure S1: Venn diagrams showing the overlap of significantly differentially expressed genes between *Atad2* KO and *Atad2* WT samples at day 26 post-partum (PP), compared with three gene sets reported by (Fontaine et al. 2022). (A) Genes upregulated in the absence of histone H3.3 in both *Atad2* WT and *Atad2* KO samples at day 26 PP. **(B)** genes repressed under the same conditions, and **(C)** sex chromosome–linked genes. In the differential expression analysis, a fold-change greater than 1.2 between *Atad2* KO and *Atad2* WT samples was considered significant.

1015 **Supplemental_Fig_S2**

1016

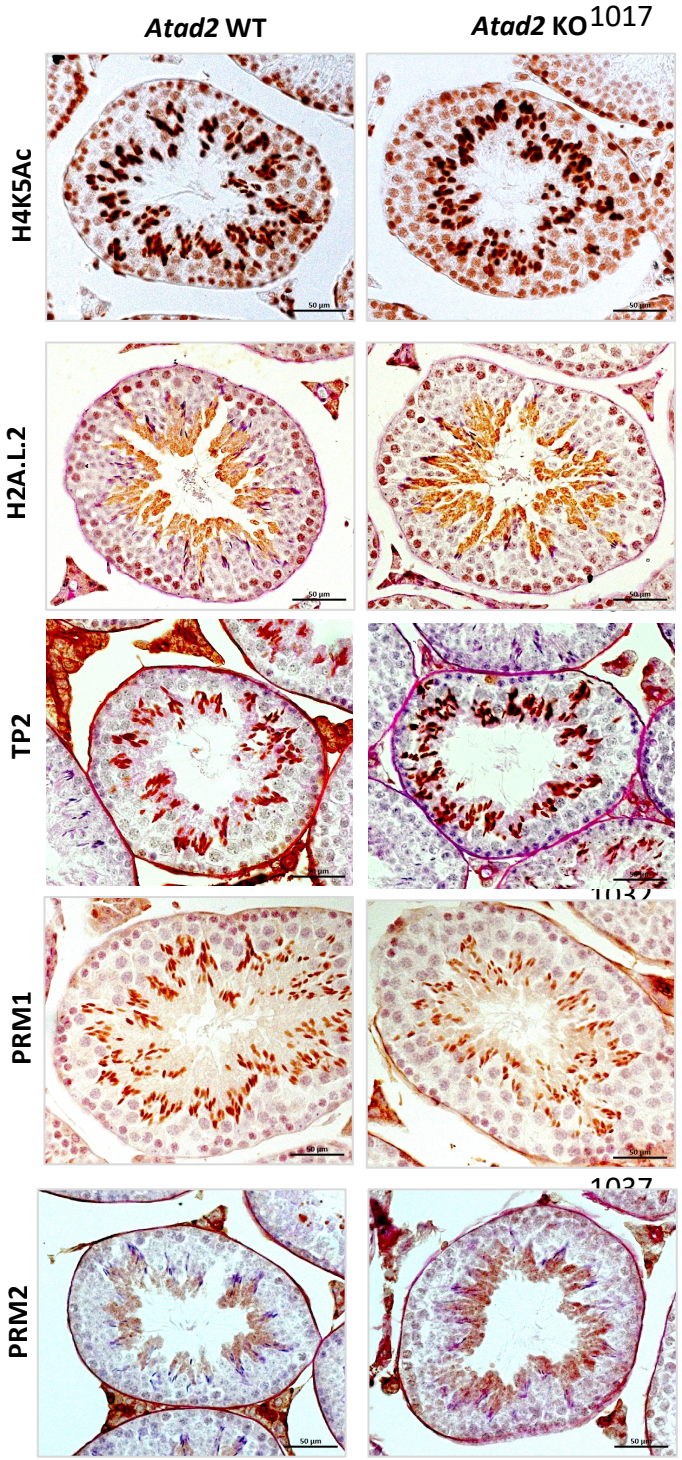

1017

1042

1043 **Figure S2: *Atad2* gene inactivation does not disrupt testis morphology, acetylation of**
1044 **H4K5ac, or the cell-specific accumulation of H2A.L.2, TP2, PRM1 and PRM2.** Paraffin-
1045 embedded sections from wild-type or *Atad2* KO testes were used to visualize the
1046 accumulation of H4K5ac or expression of H2A.L.2, TP2, PRM1 and PRM2.

1047 **Supplemental_Fig_S3**

1048

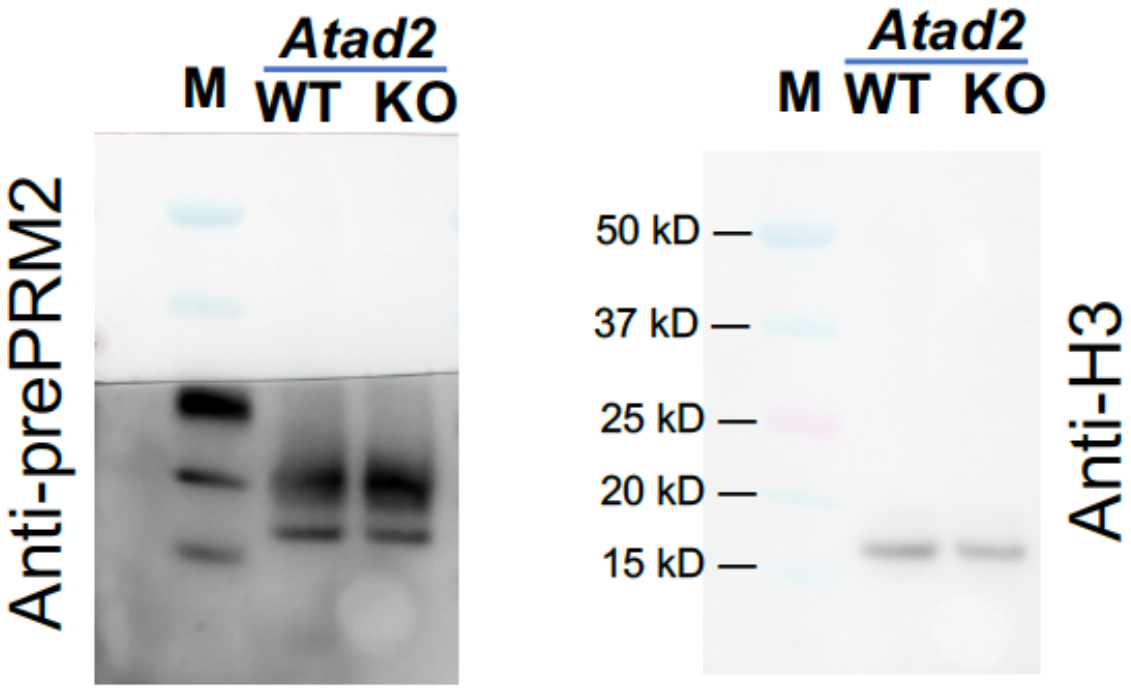

1049

1050 **Figure S3: ATAD2 is required for proper pre-protamine 2 processing.** Extracts from
1051 representative samples shown in Fig. 7B, derived from wild-type or *Atad2* KO cells, were
1052 analyzed by SDS-PAGE followed by immunoblotting using our anti-prePRM2 and anti-histone
1053 H3 antibodies. In each panel, the films were aligned with the corresponding blot and
1054 photographed. M, molecular weight marker.

1055
1056
1057
1058
1059
1060
1061
1062
1063
1064
1065
1066
1067
1068
1069
1070

Supplemental_Fig_S4.

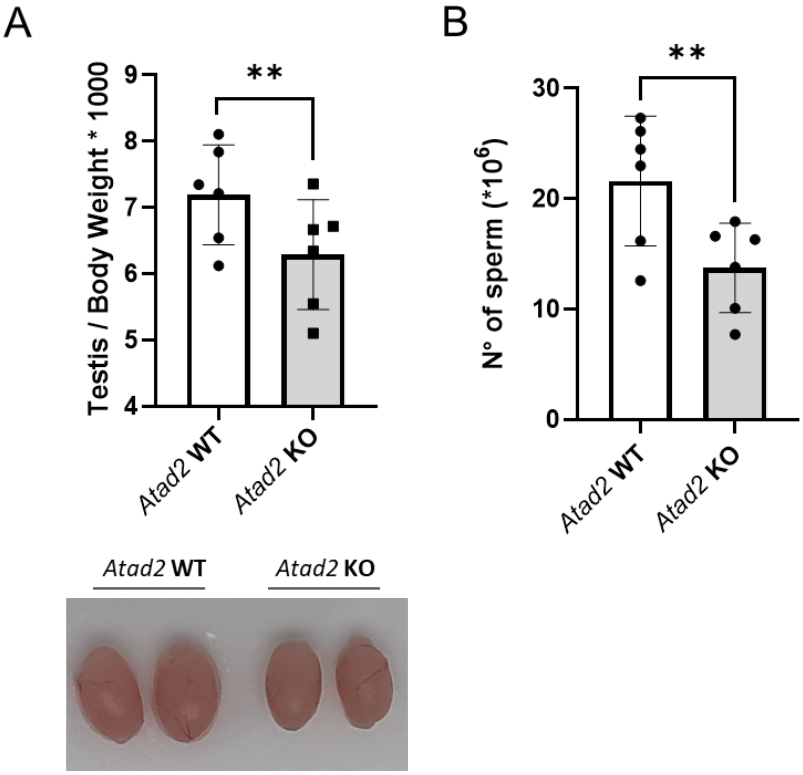

Figure S4: *Atad2* depletion affects testis weight and mature sperm counts.

(**A**) Testes from six 21- to 27-week-old wild-type and *Atad2* KO mice were collected, weighted (mg) and their weights normalized to body weight and only same-age mice were compared pairwise. Histograms represent the mean of the measured weights and error bars the Standard Deviation (upper panel). The *p*-value of pairwise Student t-test = 0.004. The lower panel shows representative testes from wild-type and *Atad2* KO mice.

(B) Spermatozoa count (Cells /ml) were performed for pairs of wild type and *Atad2* KO (*n=6*). The average numbers of spermatozoa counts are respectively 21.6 ± 5.8 and 13.7 ± 4,. and the *p*-value of paired Student t-test = 0.001.

1109 **Supplemental_Fig_S5**

1110

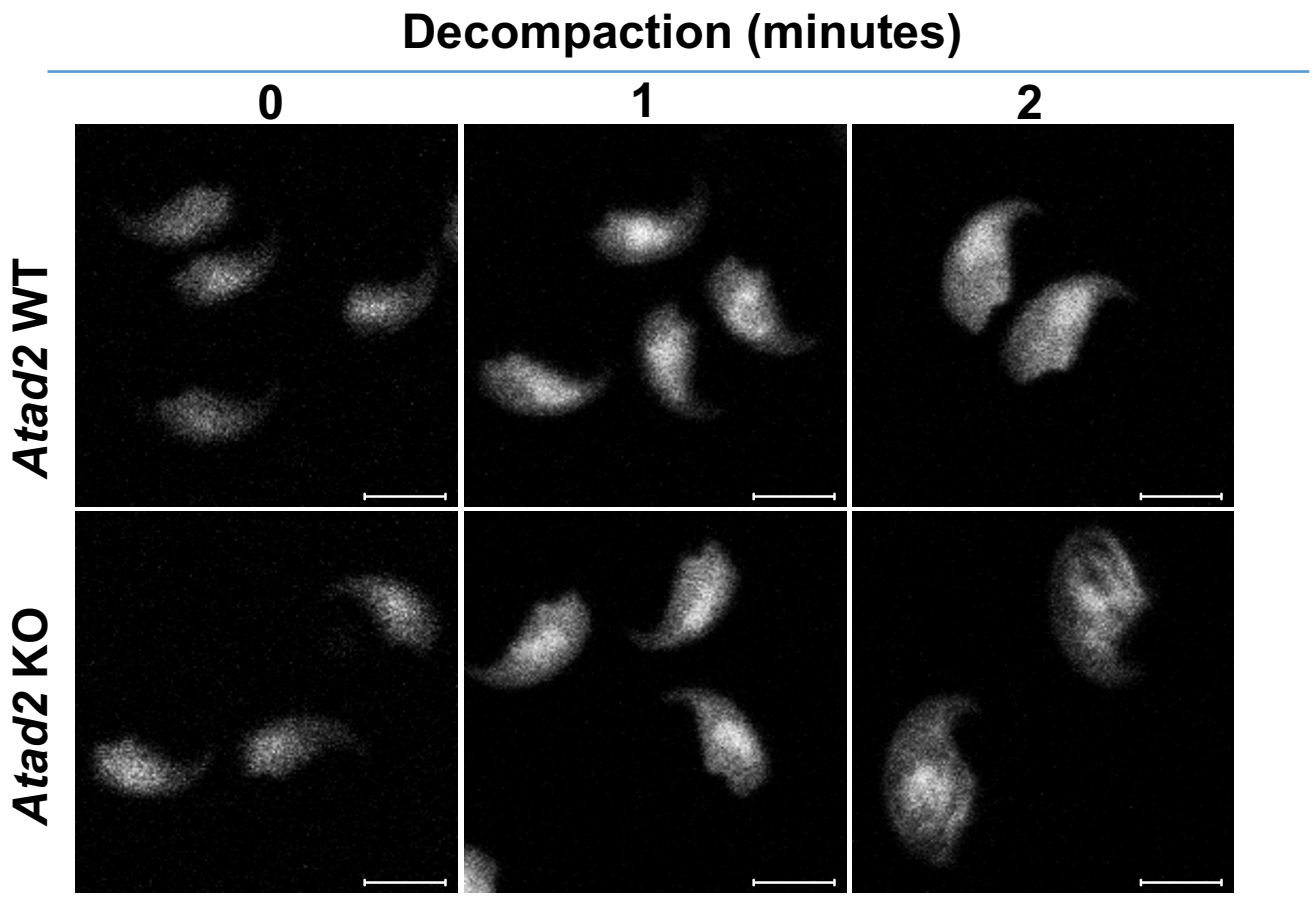

1111

1112 **Figure S5: Sperm head decompaction after DTT and heparin treatment in wild-type and**
1113 ***Atad2* KO males.** Epididymal sperm were treated with a DTT/heparin/Triton mixture, fixed,
1114 and stained with DAPI. Fluorescent images were acquired using a 63× oil-immersion objective,
1115 and sperm head size was quantified with ImageJ. Scale bars represent 5 μm.

1116
1117
1118
1119
1120
1121
1122
1123
1124
1125
1126
1127
1128
1129

1130 **Supplemental_Table_S1**

1131 **Table S1**: Primary Antibodies

Name	Company	Reference	Host Species	Dilution
Anti-ATAD2	Homemade	-	Rabbit	1:1000
anti-H2A.L1/L2 SAB771	Homemade	-	Rabbit	1:200 for IHC
Anti-Histone H3 antibody - Nuclear Marker and ChIP Grade	Abcam	Ab1791	Rabbit	1:5000 for WB
Anti-H2B (testis specific)	Abcam	AB178426	Rabbit	1:100 for IF
anti-H3F3B	Abnova	#H00003021-M01	Mouse	1:200 for IF
Anti-H4K5Ac	PTM Biolabs	#PTM-163	Mouse	1:200 for IHC
Anti-HIRA	Cell Signaling Technology	D6O8L	Rabbit	1:1000 for WB
Pre-PRM2	Homemade	-	Rabbit	1:100 for IF
anti-Protamine 1	BRIAR Patch Biosciences	HUP1N	Mouse	1:200 for IHC/IF
anti-Protamine 2	BRIAR Patch Biosciences	HUP2B	Mouse	1:200 for IHC
Anti-TNP2 (B-2)	Santa Cruz Biotechnology	sc-393843	Mouse	1:200 for IHC
Goat anti Rabbit IgG (H + L)-HRP	Bio-rad	Cat# 1706515	-	1:5000 for WB
Goat anti-Mouse IgG (H + L)-HRP	Bio-rad	Cat# 1706516	-	1:5000 for WB
Alexa Fluor™ 568 goat Anti-mouse IgG (H+L)	Invitrogen	Cat# A11004	-	1:500 for IF
Alexa Fluor™ 488 goat Anti-rabbit IgG (H+L)	Invitrogen	Cat# A11034	-	1:500 for IF

WB: Western Blot Analysis, IF: Immunofluorescence and IHC: Immunohistochemistry.

1132 **Supplemental_Table_S2**

1133 **Table S2**: Reagents / Products used

Products	Company	Reference
Bovine Serum Albumin (BSA)	Euromedex	# 04-100-812-C
Clarity™ Western ECL Substrate	Bio-Rad	Cat # 170-5061
Clarity Max™ Western ECL Substrate	Bio-Rad	Cat # 170-5062
Complete Protease inhibitor EDTA-free	Sigma-Aldrich	# 4693159001
Dako Fluorescent Mounting Medium	Dako	S3023
DL-Dithiothreitol (DTT)	Euromedex	EU0006
DNase I recombinant	Roche	4536282001
DPBS	Gibco	14200-075
Ethylenediaminetetraacetic acid disodium salt dihydrate (EDTA)	Sigma-Aldrich	E6635
Ethylene glycol-bis (2-aminoethylether)-N,N,N',N'-tetraacetic acid (EGTA)	Sigma-Aldrich	E3889
Formalin solution, neutral buffered, 10%	Sigma-Aldrich	HT5012
Glutaraldehyde solution	Sigma-Aldrich	G5882
Heparin sodium salt from porcine intestinal mucosa	Sigma-Aldrich	H3149
Hoechst	Invitrogen	# 33342
Human Chorionic Gonadotropin (HCG)	MED-VET	Chorulon 1500 UI
Laemmli Sample Buffer 4x	BioRad	# 1610747
Magnesium Chloride (MgCl2)	Euromedex	2189
Mayer's Hematoxylin Solution	Sigma-Aldrich	MHS16
M2 medium	Sigma-Aldrich	M7167
M16 medium	Sigma-Aldrich	M7292
Nitrocellulose Blotting membrane	Amersham™ Protran®	10600015
Nonidet™ P 40 Substitute (NP 40)	Sigma-Aldrich	74385
NuPAGE™ 4-12% Bis-Tris Gel	Invitrogen	NP0335BOX

Potassium Ferricyanide	Sigma-Aldrich	P-8131
Potassium Ferrocyanide	Sigma-Aldrich	P-9387
Pregnant Mare Serum Gonadotropin (PMSG)	MED-VET	Syncro-part PMSG 600 UI
Saccharose	Sigma-Aldrich	S7903
Saponin from quillaja bark	Sigma-Aldrich	S7900
Sodium deoxycholate (NaDoc)	Sigma-Aldrich	D6750
Superfrost®slides	Thermo Scientific™	LCSF05
TMB ELISA Substrate (High Sensitivity)	Abcam	AB171523
Trans-Blot Turbo 5X Transfer Buffer	BioRad	Cat # 10026938
Triton™ X-100	Sigma-Aldrich	T9284
TRIzol™	Thermo Scientific™	# 15596026
TWEEN® 20	Sigma-Aldrich	P7949
Urea	Sigma-Aldrich	U5378
X-Gal	Invitrogen	B1690
96 Well Round (U) Bottom Plate	Thermo Scientific™	# 163320
450 nm Stop Solution for TMB Substrate	Abcam	AB171529

1134
1135
1136